

Calibrating mid-infrared emission as a tracer of obscured star formation on H II-region scales in the era of JWST

Francesco Belfiore^{1,*}, Adam K. Leroy², Thomas G. Williams³, Ashley T. Barnes⁴, Frank Bigiel⁵, Médéric Boquien⁶, Yixian Cao⁷, Jérémy Chastenet⁸, Enrico Congiu⁹, Daniel A. Dale¹⁰, Oleg V. Egorov¹¹, Cosima Eibensteiner⁵, Eric Emsellem^{4,12}, Simon C. O. Glover¹³, Brent Groves¹⁴, Hamid Hassani¹⁸, Ralf S. Klessen^{13,15}, Kathryn Kreckel¹¹, Lukas Neumann⁵, Justus Neumann¹⁶, Miguel Querejeta¹⁷, Erik Rosolowsky¹⁸, Patricia Sanchez-Blazquez^{19,20}, Karin Sandstrom²¹, Eva Schinnerer¹⁶, Jiayi Sun^{22,23}, Jessica Sutter²¹, and Elizabeth J. Watkins¹¹

(Affiliations can be found after the references)

Received XXX; accepted XXX

ABSTRACT

Measurements of the star formation activity on cloud scales are fundamental to uncovering the physics of the molecular cloud, star formation, and stellar feedback cycle in galaxies. Infrared (IR) emission from small dust grains and polycyclic aromatic hydrocarbons (PAHs) are widely used to trace the obscured component of star formation. However, the relation between these emission features and dust attenuation is complicated by the combined effects of dust heating from old stellar populations and an uncertain dust geometry with respect to heating sources. We use images obtained with NIRC2 and MIRI as part of the PHANGS–JWST survey to calibrate the IR emission at $21\mu\text{m}$, and the emission in the PAH-tracing bands at 3.3 , 7.7 , 10 , and $11.3\mu\text{m}$ as tracers of obscured star formation. We analyse ~ 16000 optically selected H II regions across 16 nearby star-forming galaxies, and benchmark their IR emission against dust attenuation measured from the Balmer decrement. We model the extinction-corrected $H\alpha$ flux as the sum of the observed $H\alpha$ emission and a term proportional to the IR emission, with a_{IR} as the proportionality coefficient. A constant a_{IR} leads to an extinction-corrected $H\alpha$ estimate which agrees with those obtained with the Balmer decrement with a scatter of ~ 0.1 dex for all bands considered. Among these bands, $21\mu\text{m}$ emission is demonstrated to be the best tracer of dust attenuation. The PAH-tracing bands underestimate the correction for bright H II regions, since in these environments the ratio of PAH-tracing bands to $21\mu\text{m}$ decreases, signalling destruction of the PAH molecules. For fainter H II regions all bands suffer from an increasing contamination from the diffuse infrared background. We present calibrations that take this effect into account by adding an explicit dependence on $3\mu\text{m}$ emission or stellar mass surface density.

Key words. Galaxies: ISM – Galaxies: star formation – ISM: general

1. Introduction

Interstellar dust biases our view of star formation, obscuring the ultraviolet (UV) and optical emission of newly formed massive stars. The energy absorbed by dust at short wavelengths is re-radiated in the IR, making observations of dust emission a powerful probe of embedded star formation. Multi-wavelength studies, at both low and high redshift, have highlighted the importance of the IR to provide a full accounting of star formation rates (SFRs) in galaxies (Calzetti et al. 2007; Wuyts et al. 2011b; Kennicutt & Evans 2012; Gruppioni et al. 2013; Madau & Dickinson 2014; Calzetti 2020).

The thermal dust emission spectrum peaks in the far-IR. In the limit where the dust heating is dominated by young stellar populations, the far-IR emission can be directly related to the embedded SFR using energy balance (Kennicutt 1998). However, such a bolometric measure of dust luminosity is sensitive to heating by older stellar populations (Cortese et al. 2008). This heating term contributes progressively more to the cooler, longer wavelength far-IR emission, leading to diffuse ‘IR cirrus’. On the other hand, the mid-IR (MIR) region around $24\mu\text{m}$, corresponding to the IRAS $25\mu\text{m}$, the *Spitzer* MIPS $24\mu\text{m}$ band, or the WISE W4 ($22\mu\text{m}$) filter, traces emission of small, hot grains transiently heated by the local radiation field. While not directly related to the bolometric dust luminosity without further assumptions on the shape of the dust SED, emission at $24\mu\text{m}$ has

the advantage of tracing a hotter dust component, and therefore being less sensitive to IR cirrus.

Several authors have advocated the use of $24\mu\text{m}$ fluxes, in combination with either UV or $H\alpha$ recombination line emission, to account for both the attenuated and un-attenuated component of the SFR (Hirashita et al. 2003; Kennicutt et al. 2007; Calzetti et al. 2007; Kennicutt et al. 2009; Wuyts et al. 2011a; Hao et al. 2011; Leroy et al. 2012; Kennicutt & Evans 2012; Jarrett et al. 2013; Catalán-Torrecilla et al. 2015; Leslie et al. 2018). These hybrid recipes have been demonstrated to be successful for both integrated galaxies and kpc-scale sub-galactic regions in local galaxies (Calzetti et al. 2007; Leroy et al. 2012; Belfiore et al. 2023). However, dust heating from old stellar populations can still constitute a significant fraction of a galaxy’s integrated emission at $24\mu\text{m}$ (Bendo et al. 2012; Groves et al. 2012; Crocker et al. 2013; Lu et al. 2015; Boquien et al. 2016; Viaene et al. 2017) and complicates the association of the MIR with star formation in observations that have low spatial resolution (Leroy et al. 2012).

In addition to $24\mu\text{m}$, several authors have studied the potential of using the flux in PAH features or the brightness of PAH-tracing bands (most commonly the IRAC $8\mu\text{m}$ band) to probe obscured star formation (Peeters et al. 2004; Shipley et al. 2016; Maragkoudakis et al. 2018). These calibrations offer significant advantages with respect to the longer mid-IR wavelengths in terms of angular resolution and sensitivity (Calzetti 2020; Li 2020). Moreover, PAH features remain accessible and are read-

* e-mail: francesco.belfiore@inaf.it

ily identifiable with *Spitzer*, and now JWST, out to high redshifts (Lutz et al. 2005; Riechers et al. 2014). Studies of nearby galaxies at high spatial resolution have demonstrated, however, that PAH emission is suppressed relative to $24\ \mu\text{m}$ (or total IR) emission at the position of H II regions (Helou et al. 2004; Bendo et al. 2006; Bolatto et al. 2007; Lebouteiller et al. 2011; Chasstenet et al. 2019, 2023b; Egorov et al. 2023). In particular, PAH emission is found to generate bright rings around H II regions, probably due to PAH photo-destruction, therefore complicating the relation between PAHs and star formation (Galliano et al. 2018).

In this work, we test the use of both the MIR dust continuum at $21\ \mu\text{m}$ and bands dominated by PAH emission to trace embedded star formation on the scale of individual H II regions ($\sim 40\text{--}110\ \text{pc}$) in a sample of 16 nearby disc galaxies observed with the MIRI and (partially) with NIRCam instruments onboard JWST as part of the PHANGS (Physics at High Angular resolution in Nearby Galaxies) JWST program (Lee et al. 2023). We compare the attenuation estimates obtained using literature calibrations based on the MIR/H α ratios with matched-resolution Balmer decrement (H α /H β) measurements obtained from the PHANGS–MUSE integral field spectroscopy (IFS) mapping with the VLT/MUSE instrument (Emsellem et al. 2022).

Using this JWST data we calibrate photometric measurements of the MIR continuum and PAH emission to accurately trace the obscured component of star formation on scales of individual H II regions. Our analysis builds on the work of Leroy et al. (2023b) and Hassani et al. (2023), who used early data for a subset of four galaxies in our sample to demonstrate that attenuation-corrected H α emission correlates well with MIR emission at $21\ \mu\text{m}$, albeit non-linearly, for regions that are bright in the MIR.

In Sec. 2 we present our data, paying special attention to the new JWST images, and summarise the methods for inferring the dust attenuation. In Sec. 3 we present our results concerning the use of the IR bands in correcting H α for dust attenuation in H II regions, and discuss the recommended recipes and potential future work in Sec. 4. We summarise the results in Sec. 5.

2. Data and Methods

2.1. PHANGS–JWST data

We analysed 16 galaxies observed as part of the cycle 1 PHANGS–JWST Treasury program (ID 02107, PI: J. Lee). The full survey will consist of MIRI and NIRCam images for the 19 nearby galaxies observed by the PHANGS–MUSE survey (Emsellem et al. 2022). The data used in this work corresponds to the subset of the PHANGS–JWST program available at the time of writing. Key properties of our 16 target galaxies are summarised in Table 1.

For each target we obtained one or more NIRCam and MIRI tiles, covering roughly the same area on sky and maximising the overlap with existing MUSE observations. MIRI images were obtained in the F770W, F1000W, F1130W and F2100W filters, centred at 7.7, 10, 11.3, and $21\ \mu\text{m}$, respectively. With NIRCam we obtained images in the F200W, F300M, F335M, and F360M filters, centred at 2.0, 3.0, 3.37, and $3.6\ \mu\text{m}$, respectively. NIRCam and MIRI observations were obtained in sequence, in order to obtain a MIRI background pointing in parallel with the NIRCam observations. However, for three galaxies (IC 5332, NGC 4303, NGC 4321) all or part of the NIRCam observations were not obtained due to guide star failures.

In the case of IC 5332 no NIRCam data was obtained, while for NGC 4303 and NGC 4321 only one NIRCam tile was obtained out of the intended two-tile mosaic, therefore covering roughly half of the area imaged with MIRI. In the case of IC 5332 no MIRI background pointing is available, so the background frame for NGC 7496 (taken on the same day) was used.

The observing strategy and data reduction workflow are presented in Lee et al. (2023), while Leroy et al. (2023b) discuss the determination and anchoring of the background level for the MIRI imaging. We briefly discuss updates with respect to the reduction procedure implemented in those works. Firstly, we used the latest version of the CRDS context (jwst_1070) and science calibration pipeline (v1.10.0). Secondly, we have implemented a custom background matching technique to minimise the per-pixel difference in each pair of overlapping tiles. The JWST pipeline assumes a constant background across the image, which is not the case for our observations (in many cases, one half of the image has a significantly lower ‘background’ level than the other). Our routine avoids this by calculating the median per-pixel difference in each overlapping pair, and finding values that minimise this across the tile set. Thirdly, we have improved the absolute astrometry for the long wavelength MIRI tiles, by basing the astrometric solution of the longer bands on that of the shortest MIRI band (F770W). As each tile in each filter is observed close in time, and using the same guide stars, this produces significantly better astrometric solutions than attempting to match each band separately. Finally, as discussed in Leroy et al. (2023b) the background level of the overall image mosaics are re-scaled to match those of existing *Spitzer* or WISE data. This step is necessary because we generally do not have empty sky regions that can be used for background subtraction within our mosaics. Further details of the reduction strategy will be described in an upcoming publication from the PHANGS–JWST team.

We convolved the JWST images to match the MUSE point spread function (PSF), which is different for each target as discussed in the next subsection. The required kernels were generated using the methodology of Aniano et al. (2011) and the JWST PSFs were obtained via the WebbPSF tool (Perrin et al. 2014). Error maps produced by the JWST reduction pipeline were also convolved with the same kernels and the errors are propagated analytically through the convolution process. For 15 of the 16 targets the MUSE PSF is larger than that of the lowest-resolution JWST band in our filter set (F2100W). For one galaxy, NGC 4535, the MUSE PSF full width at half maximum (FWHM) ($0.56''$) is smaller than the F2100W PSF. We therefore convolve the JWST data with the smallest suitable kernel (an ‘aggressive’ kernel in the definition of Aniano et al. 2011) to generate an image with a Gaussian PSF. The resulting PSF FWHM is of $0.71''$ FWHM, and the MUSE maps for this galaxy are smoothed to the same PSF.

In the NIRCam wavelength range, the PAH emission feature at $3.3\ \mu\text{m}$ falls in the F335M medium-band filter. As discussed in Sandstrom et al. (2023a), we performed a bespoke continuum subtraction procedure using the adjoining F300M and F360M medium-band filters in order to remove stellar continuum emission and minimise the impact of the PAH emission contaminating the F360M side-band. Our procedure is based on and improves upon the scheme first suggested by Lai et al. (2020). In this work we refer to the resulting continuum-subtracted emission as

$$F335M_{\text{PAH}} = F335M - F335M_{\text{cont}}, \quad (1)$$

where $F335M_{\text{cont}}$ is the continuum contamination estimated using equations 10 and 11 from Sandstrom et al. (2023a). For the rest of this work we only work with the continuum-subtracted $F335M_{\text{PAH}}$ band.

The data for a few galaxies necessitated further by-hand masking of prominent diffraction spikes (NGC 1365, NGC 1566, NGC 7496) caused by bright AGN, evident in the F2100W images presented in Fig. 1, further described below.

2.2. MUSE data and the optical H II region catalog

We compare the JWST images with maps of $H\alpha$ and $H\beta$ obtained with IFS from the PHANGS–MUSE program (Emsellem et al. 2022), and the associated H II region masks (Groves et al. 2023). In short, individual MUSE pointings (field of view of $1' \times 1'$) were convolved with a kernel chosen to generate a common Gaussian PSF across each galaxy mosaic which is also constant as a function of wavelength. We refer to the resulting PSF as convolved-optimised or ‘copt’. We adopt this copt FWHM as the target resolution for the JWST images, except in the case of NGC 4535 already noted above. Table 1 summarises the adopted FWHM resolution for each galaxy.

H II region masks were derived with the `HIIPHOT` algorithm (Thilker et al. 2000), which separates nebulae from the surrounding emission by first defining seed regions around bright peaks, and extending them until a termination gradient in the surface brightness profile is reached. Line fluxes and key nebular properties (e.g. metallicity, ionisation parameter) were derived within each H II region integrating the spectra inside the mask following the procedure detailed in Groves et al. (2023).

Fluxes in each JWST band were extracted within our H II region masks by reprojecting the JWST images onto the MUSE astrometric grid. Regions only partially covered by the footprint of the MIRI data or including masked or saturated pixels were discarded. Since the MIRI and NIRCcam coverage in each target is not identical, and some targets lack NIRCcam data coverage, some H II regions have MIRI fluxes but lack NIRCcam ones, or vice versa. In general, for each section of the analysis we use all H II regions with valid JWST data, leading to a slightly different sample of regions when different bands are considered. We have checked that restricting the analysis to H II regions that have valid fluxes in all JWST bands does not alter the results.

No local background subtraction was performed in our fiducial analysis because of the substantial crowding of sources and the resulting uncertainty intrinsic to a local background definition. However, we test the impact of this choice by performing a simple local background subtraction for each H II region. We define the background as the mean surface brightness in an annulus around each region two MUSE pixels (each pixel is $0.2''$) distant from the region boundary and three pixels in width. If such an annulus overlaps with other regions, we remove the overlap area from the background mask. This procedure is simplistic and leads to fairly large background levels. For example, at $21\mu\text{m}$ 25% of the H II regions in our sample have fluxes consistent with the local background with their error, and the average contrast between the flux in the H II regions and in the background is 1.5. Because of the fairly arbitrary choices involved in the definition of a background level, we focus instead on the analysis of H II region fluxes without background subtraction throughout this work, but we comment in the text and tables on the effect of the background subtraction, where relevant.

When considering the properties of H II regions we further applied cuts in the BPT (Baldwin–Phillips–Terlevich, Baldwin et al. 1981; Phillips et al. 1986) diagrams $[N\text{II}]/H\alpha$ versus

$[O\text{III}]/H\beta$ and $[S\text{II}]/H\alpha$ versus $[O\text{III}]/H\beta$, corresponding to the dividing lines of Kauffmann et al. (2003), and Kewley et al. (2001), respectively, to minimise contamination from supernova remnants and planetary nebulae (Groves et al. 2023). This excluded 25% of the starting sample of nebulae. Finally, we discarded regions overlapping with foreground stars (0.3%), or that have a signal-to-noise ratio lower than three in $H\alpha$ or $H\beta$ (0.4%). We obtain a final sample of 16 474 regions with signal-to-noise ratio larger than three in F2100W. Their distribution across the sample is summarised in Table 1.

2.3. Balmer decrement and extinction correction

The attenuation correction using the Balmer decrement is computed assuming Case B recombination, temperature $T = 10^4$ K and density $n_e = 10^2 \text{ cm}^{-3}$, leading to $I_{H\alpha, \text{corr}}/I_{H\beta, \text{corr}} = 2.86$ (Osterbrock & Ferland 2006). Under these assumptions

$$E(B - V) = \frac{2.5}{k_{H\beta} - k_{H\alpha}} \log_{10} \left[\frac{I_{H\alpha}/I_{H\beta}}{2.86} \right], \quad (2)$$

where $k_{H\alpha}$ and $k_{H\beta}$ are the value of the assumed reddening curve at the wavelengths of the two emission lines. We assume a foreground attenuation law following O’Donnell (1994).

In order to minimise the effect of distance (and correlated distance uncertainties) across our sample, we present results for H II regions in terms of luminosity per unit area, and in the following $I_{H\alpha}$, $I_{H\alpha, \text{corr}}$ and I_{band} refer to the luminosity per unit area of observed $H\alpha$ emission, Balmer decrement corrected $H\alpha$, and one of the JWST bands, all in units of $\text{erg s}^{-1} \text{ kpc}^{-2}$.

The range of distances covered by the sample (from 5.2 to 19.6 Mpc) may affect the amount of background contamination, although within our small sample we cannot identify a distance-related change in the relations we study in the rest of this work. Values of luminosity per unit area are corrected by a factor of $\cos i$, where i is the galaxy inclination, to account for projection effects (Lang et al. 2020, Table 1). Since our sample excludes highly inclined galaxies, not performing this correction has minimal impact on the results.

2.4. Other ancillary data

Throughout this work we use a number of additional physical quantities to characterise H II regions and their local environments. We summarise the definitions, data sets leveraged, and the publications where each of these physical quantities were first derived in Table 2.

In particular, we define a specific star-formation rate (sSFR) at the location of our H II regions from the attenuation-corrected $H\alpha$ assuming full sampling of the IMF, to allow for a direct comparison with the work of Belfiore et al. (2023). We define

$$\log(\text{sSFR}/\text{yr}^{-1}) = C_{H\alpha} I_{H\alpha, \text{corr}}/\Sigma_{\star}, \quad (3)$$

where $C_{H\alpha}$ is the conversion factor derived for a fully-sampled initial mass function (IMF) by Calzetti et al. (2007), and Σ_{\star} is the stellar mass surface density estimated from the MUSE data at the location of the H II region, corrected downwards by 0.09 dex to bring it into agreement with the stellar masses obtained by Salim et al. (2018) and Leroy et al. (2019) based on SED fitting (see discussion in Belfiore et al. 2023). This stellar mass surface density estimate does not refer to the mass of the cluster ionising the H II region, which cannot be resolved in the MUSE data, but is derived in larger spatial bins, of size comparable to the copt PSF FWHM (Emsellem et al. 2022).

Galaxy	D [Mpc]	$\log(M_\star)$ [M_\odot]	$\log(\text{SFR})$ [$M_\odot \text{ yr}^{-1}$]	i [deg]	Copt PSF [arcsec]	θ_{bm} [pc]	N_{HII}	Notes
IC 5332	9.0	9.67	-0.39	26.9	0.87	38	546	no NIRCcam
NGC 0628	9.8	10.34	0.24	8.9	0.92	44	1711	grand-design spiral
NGC 1087	15.9	9.93	0.12	42.9	0.92	71	910	
NGC 1300	19.0	10.62	0.07	31.8	0.89	82	946	nuclear ring
NGC 1365	19.6	10.99	1.23	55.4	1.16	109	555	AGN, nuclear ring
NGC 1385	17.2	9.98	0.32	44.0	0.77	64	912	
NGC 1433	18.6	10.87	0.05	28.6	0.91	82	849	nuclear ring
NGC 1512	18.8	10.71	0.11	42.5	1.25	114	477	nuclear ring
NGC 1566	17.7	10.78	0.66	29.5	0.80	69	1561	AGN
NGC 1672	19.4	10.73	0.88	42.6	0.96	90	934	AGN, nuclear ring
NGC 3627	11.3	10.83	0.58	57.3	1.05	58	973	AGN
NGC 4303	17.0	10.52	0.73	23.5	0.78	64	2042	AGN, nuclear ring, NIRCcam covers half
NGC 4321	15.2	10.75	0.55	38.5	1.16	86	1239	nuclear ring, NIRCcam covers half
NGC 4535	15.8	10.53	0.33	44.7	0.71*	54	1101	AGN
NGC 5068	5.2	9.40	-0.56	35.7	1.04	26	1182	
NGC 7496	18.7	10.00	0.35	35.9	0.89	81	536	AGN

Table 1. Distances are taken from the compilation of [Anand et al. \(2021\)](#), stellar mass and SFR are from [Leroy et al. \(2021b\)](#), inclinations from [Lang et al. \(2020\)](#) where available, otherwise from [Leroy et al. \(2021b\)](#), and PSF FWHM of the copt MUSE data are from [Emsellem et al. \(2022\)](#) (* for this galaxy the copt FWHM is smaller than the F2100W PSF, so we used an ‘aggressive’ kernel to convolve the JWST data to a Gaussian PSF). θ_{bm} gives the size of the common resolution element with no inclination correction. N_{HII} gives the number of HII regions from [Groves et al. \(2023\)](#) overlapping with the MIRI footprint, detected in F2100W, and meeting our other selection criteria (see text). The notes include information on which galaxies have missing or partial coverage with NIRCcam.

Quantity	Definition	Derived from dataset	Reference
Σ_{H_2}	$\alpha_{\text{CO}} I_{\text{CO}(2-1)} / R_{21}^{\text{a}}$	ALMA	Leroy et al. (2021b)
$E(B - V)$	Eq. 2	MUSE	Groves et al. (2023)
Σ_\star	spectral fitting	MUSE	Emsellem et al. (2022)
sSFR	$C_{\text{H}\alpha} I_{\text{H}\alpha, \text{corr}} / \Sigma_\star^{\text{b}}$	MUSE	Belfiore et al. (2023)
$\text{EW}(\text{H}\alpha)$	moments of spectra ^c	MUSE	Groves et al. (2023)
$12 + \log(\text{O}/\text{H})$	Scal calibration ^d	MUSE	Groves et al. (2023)
$\log(\text{U})$	from $\frac{[\text{SIII}]\lambda\lambda 9069, 9532}{[\text{SII}]\lambda\lambda 6717, 31}^{\text{e}}$	MUSE	Groves et al. (2023)

Table 2. Summary of additional data and physical quantities used in this work.

Notes. **a:** assuming a Milky Way conversion factor $\alpha_{\text{CO}} = 4.35 M_\odot \text{ pc}^{-2} (\text{K km s}^{-1})^{-1}$ ([Bolatto et al. 2013](#)) and a CO(2-1)-to-CO(1-0) ratio $R_{21} = 0.65$ ([Den Brok et al. 2021](#)). **b:** $\log C_{\text{H}\alpha} / (M_\odot \text{ yr}^{-1} / (\text{erg s}^{-1})) = -41.26$, from [Calzetti et al. \(2007\)](#). **c:** definition in [Westfall et al. \(2019\)](#). **d:** Scal calibration from [Pilyugin & Grebel \(2016\)](#). **e:** ionisation parameter calculated using the calibration from [Diaz et al. \(1991\)](#).

In addition, in Sec. 3.1.3 we use the molecular gas mass surface density, as traced by CO(2-1) maps obtained as part of the PHANGS-ALMA program ([Leroy et al. 2021a,b](#)), at the positions of our optically defined H II regions. The ALMA data has slightly lower angular resolution than copt ($\sim 1.3''$) for each of our galaxy targets, but considering the integration over the H II region masks the small mismatch in resolution does not affect our results.

3. Results

3.1. Using 21 μm emission as a tracer of obscured star formation

We aim to provide attenuation-corrected measures of the ionising photon luminosity from massive stars to trace recent star formation in individual H II regions. To do so, we follow the well-established approach of using the MIR to correct for the obscured part of the H α luminosity ([Hirashita et al. 2003](#); [Calzetti et al. 2007](#); [Kennicutt et al. 2009](#); [Belfiore et al. 2023](#)). Taking the MIRI F2100W band centred at 21 μm as our fiducial band,

we can write the attenuation-corrected H α luminosity per unit area as

$$I_{\text{H}\alpha, \text{corr}}^{\text{hybrid}} = I_{\text{H}\alpha} + a_{21} I_{21}, \quad (4)$$

where all luminosities are expressed in units of $\text{erg s}^{-1} \text{ kpc}^{-2}$ (i.e., $I_{21} = \nu_{21} I_\nu$) and a_{21} is a dimensionless coefficient. This coefficient is generally calibrated empirically because of its complex dependence on star-formation history, star-dust geometry, shape of the dust attenuation law, and potential non-linearity in the dust emissivity with radiation field strength. The dust attenuation at the wavelength of H α can therefore be related to the $I_{21}/I_{\text{H}\alpha}$ ratio via

$$A_{\text{H}\alpha} = 2.5 \log(1 + a_{21} I_{21}/I_{\text{H}\alpha}). \quad (5)$$

An equivalent formalism can be used with the PAH-tracing bands (Sec. 3.2).

As a starting point for our analysis we consider the numerical value of the coefficient obtained by [Calzetti et al. \(2007\)](#)

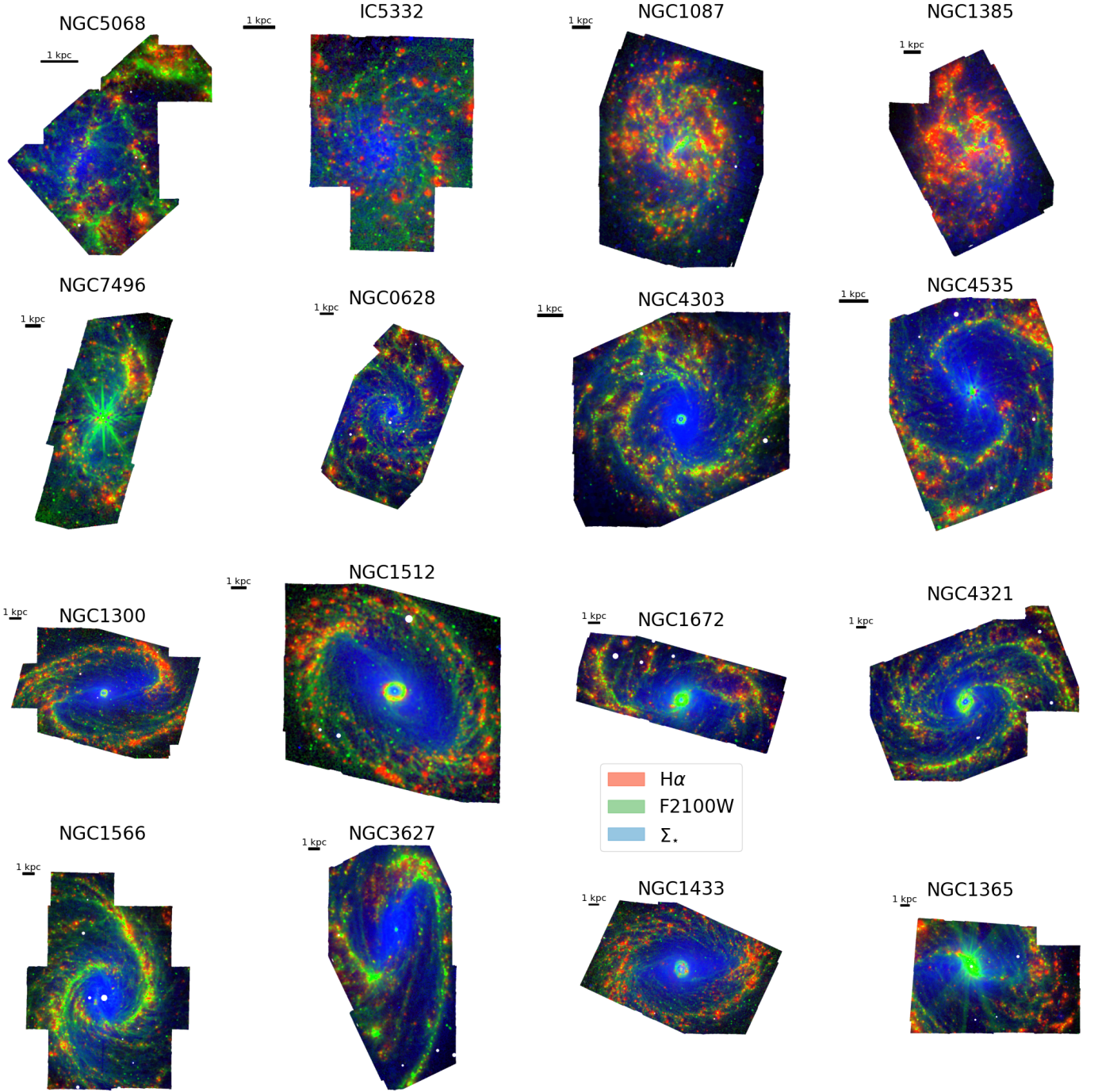


Fig. 1. Three-colour images for the 16 galaxies in our sample showing a combination of $H\alpha$ emission from MUSE IFS (red), $21\ \mu\text{m}$ emission from JWST MIRI F2100W images (green), and stellar mass surface density from MUSE full spectral fitting (blue). The JWST data and MUSE data are shown at matched resolution. Galaxies are shown in order of increasing stellar mass. Foreground stars and the AGN in NGC 1566 and NGC 1365 are masked. The diffraction spikes due to bright AGN in NGC 4535, NGC 7496 and NGC 1365 are shown here but masked in subsequent analysis. The jagged edges of the images are caused by the intersection between the MUSE and MIRI image coverage.

for a sample of star-forming complexes in nearby galaxies using *Spitzer* $24\ \mu\text{m}$ MIPS data: $a_{24}^{C07} = 0.031$. To apply this to JWST data we take into account the different filter bandpasses between MIPS $24\ \mu\text{m}$ and MIRI F2100W using the average flux ratio observed across our sample and tabulated by Leroy et al. (2023b), $\langle I_{21}/I_{24} \rangle = 0.91$, leading to $a_{21}^{C07} = 0.034$.

3.1.1. $21\ \mu\text{m}$ emission in $H\text{II}$ regions and the diffuse component

In this section we present the relative spatial distribution of $21\ \mu\text{m}$ and $H\alpha$ emission. In Fig. 1 we show three-colour images combining $H\alpha$ from MUSE (red) with $21\ \mu\text{m}$ emission from MIRI at copt resolution (green) and stellar mass surface density from MUSE full-spectral fitting (blue). Galaxies are ordered by increasing total stellar mass. The figure highlights the variety of

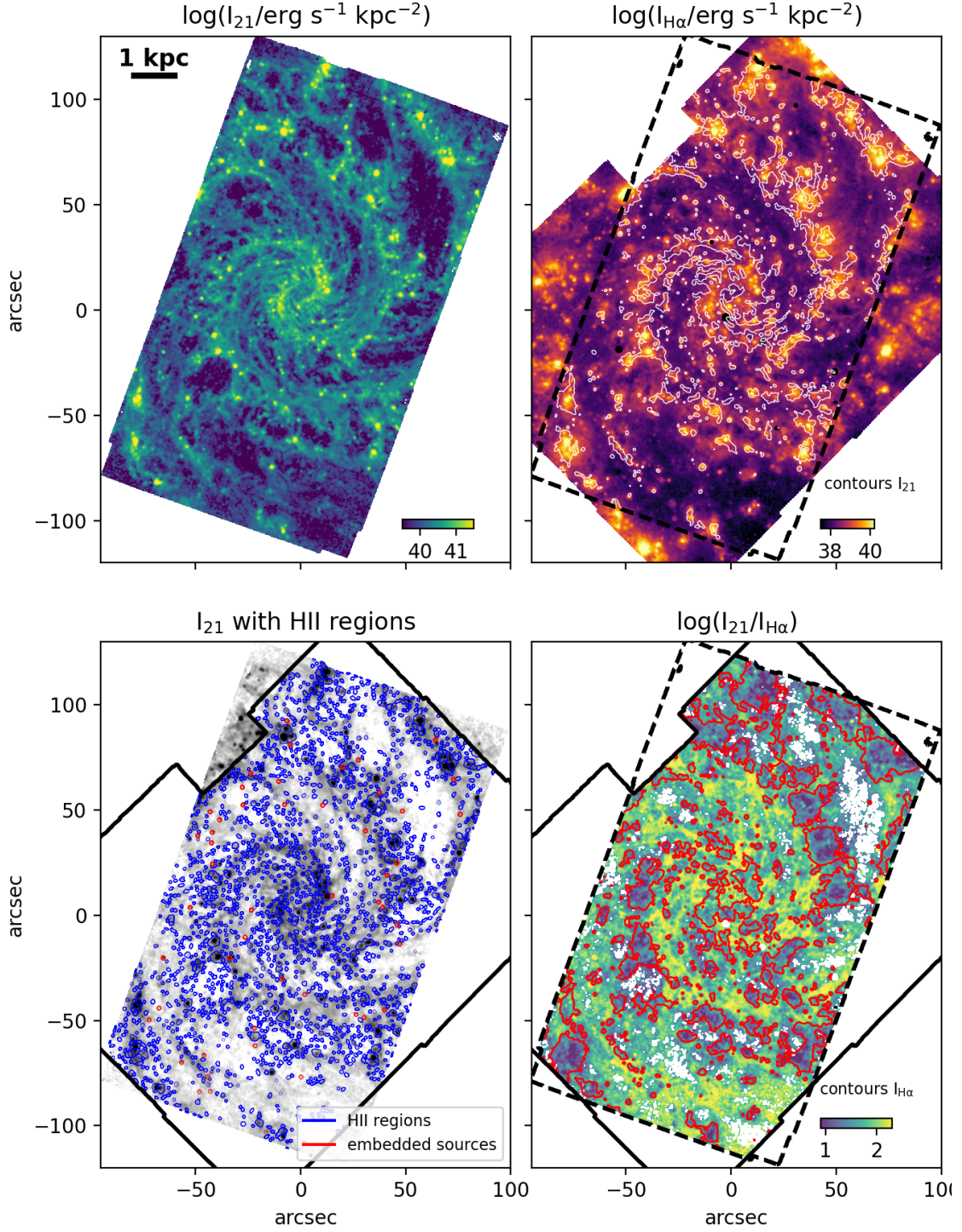


Fig. 2. Comparison of the $H\alpha$ and $21\mu\text{m}$ emission for NGC 0628. Top-left, $21\mu\text{m}$ surface brightness image obtained using the F2100W filter on MIRI, convolved to the MUSE copt resolution ($0.92''$). Top-right, map of the $H\alpha$ surface brightness from MUSE (Emsellem et al. 2022). White contours enclose regions of bright $21\mu\text{m}$ emission ($I_{21} > 10^{40.5} \text{ erg s}^{-1} \text{ kpc}^{-2}$). Bottom-left: Same as top-left, but with the boundaries of the optically selected HII regions from Groves et al. (2023) in blue and the $21\mu\text{m}$ sources which do not overlap with optical HII regions from Hassani et al. (2023) in red. Bottom-right: Ratio map of the $H\alpha$ to F2100W surface brightness. Red contours are bright $H\alpha$ regions, $I_{H\alpha} > 10^{38.8} \text{ erg s}^{-1} \text{ kpc}^{-2}$. White regions within the mapped area represent areas with $S/N < 3$ in F2100W. The boundaries of the MUSE (solid black) and MIRI (dashed black) mosaics are shown to aid in visualising the data overlap.

stellar and ISM morphologies present in our sample. Throughout the sample we observe a strong spatial correlation between bright $21\mu\text{m}$ sources and bright $H\alpha$ emission, as expected if both components are powered by young stars (and dust atten-

uation is moderate, see discussion in Leroy et al. 2023b). The fainter $21\mu\text{m}$ emission outside HII regions appears filamentary, suggesting that such emission traces primarily changes in the column density of cold gas illuminated by the diffuse interstellar

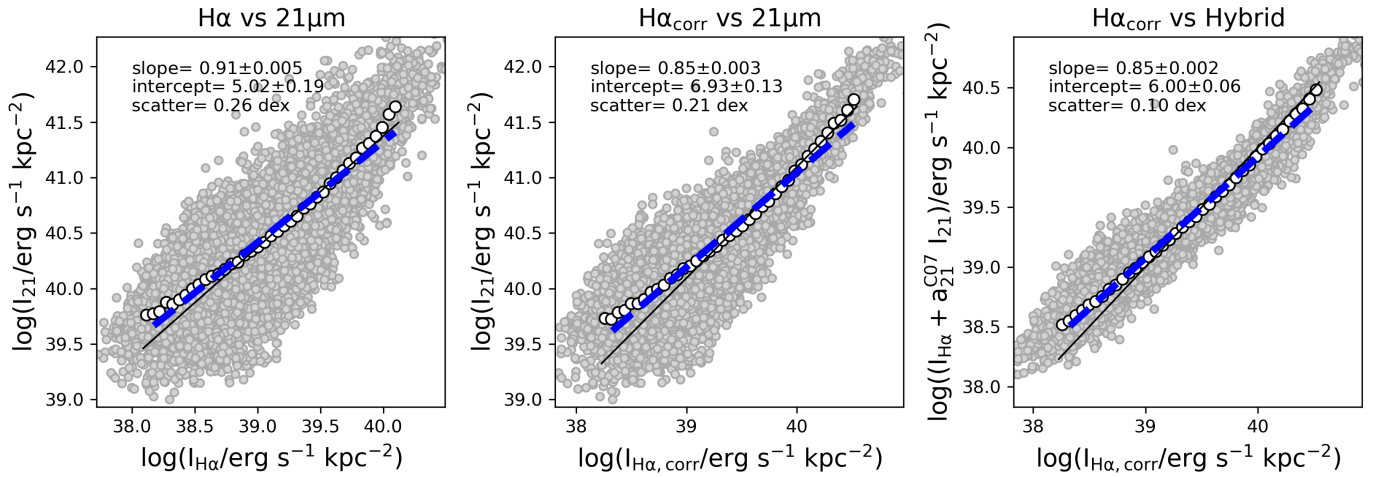


Fig. 3. Left: I_{21} as a function of $I_{H\alpha}$ for the H II regions (grey points) in our sample. The white dots represent the median relation, while the blue dashed line is the best-fit power law obtained by fitting the data considering the errors associated with the quantities on both axes. The solid black line shows a linear relation normalised to match the data at high surface brightness. The slope and intercept of the best-fit power law together with the scatter with respect to the best model are reported in the top left corner. The meaning of the symbols and lines is the same across the three panels, except that the solid black line the right panel represents a one-to-one relation. Middle: I_{21} as a function of $I_{H\alpha,corr}$. Right: $I_{H\alpha} + a_{21}^{C07} I_{21}$ as a function of $I_{H\alpha,corr}$.

radiation field (Leroy et al. 2023b; Sandstrom et al. 2023b). The presence of diffuse H α , on the other hand, correlates spatially with the positions of H II region, and can largely be attributed to leaking ionising radiation (Belfiore et al. 2022).

To discuss the relation between H α and 21 μ m emission more quantitatively we focus on one of the galaxies in our sample, NGC 628, a grand-design spiral galaxy with $\log(M_{\star}/M_{\odot}) = 10.3$. Fig. 2 (top row) presents a comparison between the 21 μ m and H α maps for NGC 628 at matched (copt) resolution. To quantify the spatial differences between H α and 21 μ m emission we compute the 21 μ m flux within and outside the optically defined H II region masks (blue contours in Fig. 2, bottom left). We find that in NGC 628, 54% of the 21 μ m emission, but only 36% of the H α emission, lies outside the H II region masks. Across the full sample the fraction of 21 μ m flux outside H II regions is on average $\sim 60\%$. This fraction is higher than the fraction of diffuse H α , which averages to 38%.

The large amount of 21 μ m emission outside H II regions is not due to a population of fully embedded star-forming regions, which may have eluded our optical catalogs. To demonstrate this, we match the MUSE H II region catalog with the catalog of 21 μ m compact point sources from Hassani et al. (2023) for the four galaxies in common (IC 5332, NGC 628, NGC 1365, NGC 7496). For this sub-sample we identify 21 μ m sources which do not overlap MUSE H II regions. We allow a maximum overlap of 10% in area and require sources to have MIR colours typical of the ISM, in order to exclude background galaxies and dusty stars (the selection criteria are discussed in Hassani et al. 2023). While the vast majority of 21 μ m point sources overlap with H II regions, in NGC 628 we find 53 non-overlapping sources, accounting for 0.7% of the total 21 μ m emission (shown as red circles in Fig. 2, bottom left). These sources do not overlap with supernova remnants or planetary nebulae in the Groves et al. (2023) catalog, so we consider them likely fully embedded star-forming regions. Over the sub-sample of four galaxies in common with Hassani et al. (2023) we find that the fraction of 21 μ m emission in such embedded point sources is of the or-

der of a few percent. Their contribution is therefore negligible in explaining the diffuse 21 μ m emission.

The difference in diffuse fraction between H α and 21 μ m emission implies that areas that are faint in H α show a higher $I_{21}/I_{H\alpha}$ ratio. In the bottom-right panel of Fig. 2 we show a ratio map of $I_{21}/I_{H\alpha}$ with red contours corresponding to regions of bright H α emission¹. The higher $I_{21}/I_{H\alpha}$ in the DIG with respect to H II regions does not imply, however, that the diffuse component suffers from a higher dust attenuation, as may be expected from a naive application of Eq. 5. In fact, the 21 μ m and H α emission are powered by different components of the radiation field, and the observed change in the ratio likely reflects differences in the radiation field rather than dust attenuation. The diffuse H α is mostly the result of the leakage of ionising photons from H II regions, with a small (few percent) contribution from old stars (Belfiore et al. 2022). The 21 μ m emission, on the other hand, is powered by UV and optical light escaping star-forming regions but also originating from the old stellar population, with this ratio changing as a function of local environment (De Looze et al. 2014; Williams et al. 2019). In this work we therefore focus entirely on the emission properties of H II regions, where both dust and H α should be powered by the same sources. The contamination from the diffuse component is, however, likely to affect the measured properties of the fainter H II regions. A more detailed study of the diffuse infrared emission and its dependence on local environment will instead be presented in a future publication. For the remainder of this work we focus on calibrating the dust correction measures for H II regions.

3.1.2. H II region scaling relations at 21 μ m

We test the framework for dust attenuation correction presented in Sect. 3.1 on the scale of H II regions using the JWST F2100W band. We start by presenting the relation between the observed

¹ $\log(I_{H\alpha}/\text{erg s}^{-1} \text{kpc}^{-2}) > 38.8$, chosen to correspond to the 16th percentile of the surface brightness distribution of H II regions in the PHANGS-MUSE sample from Belfiore et al. (2022).

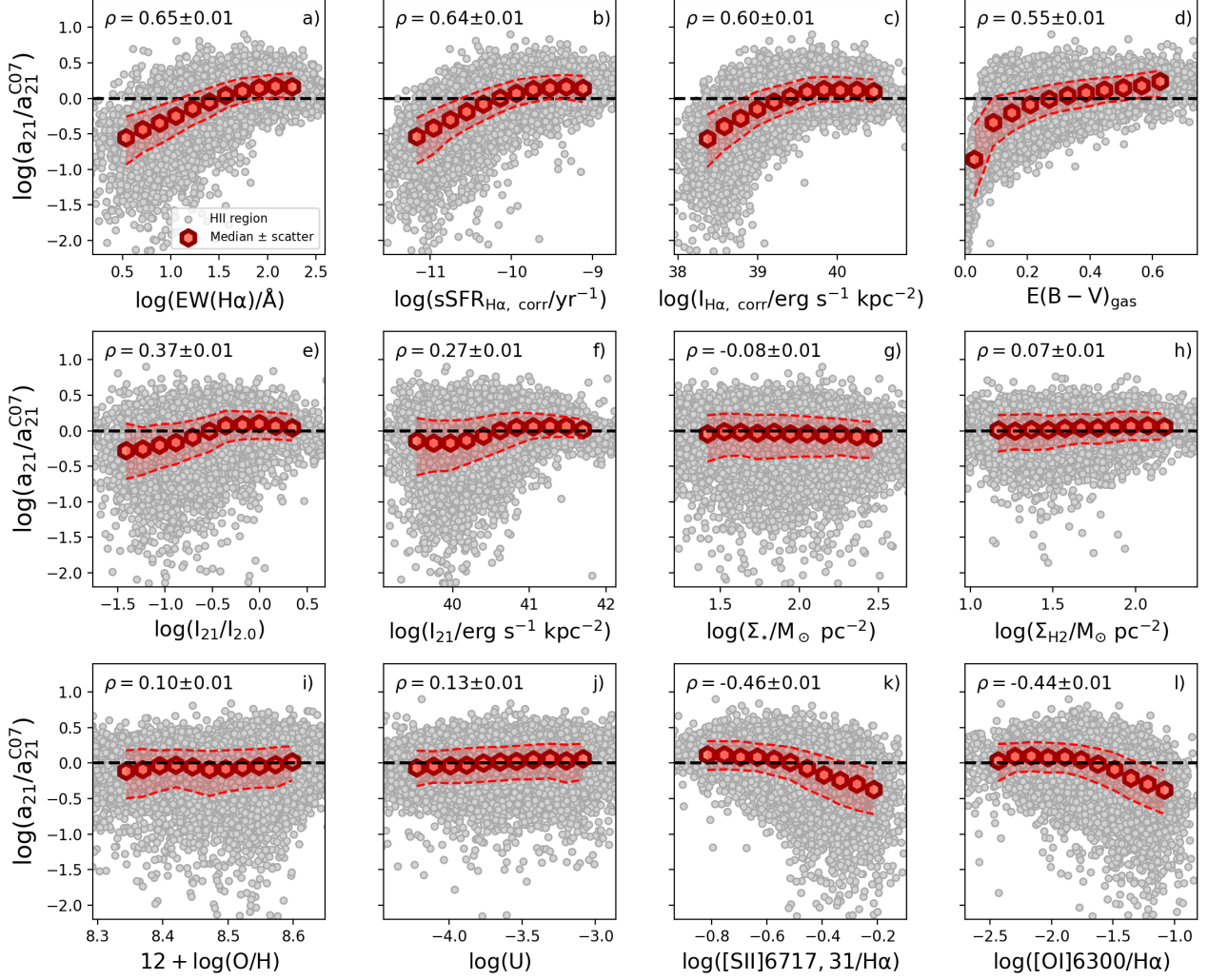


Fig. 4. The measured coefficient a_{21} normalised to the (rescaled) value from Calzetti et al. (2007) for H II regions as a function of several physical properties. Grey points are individual H II regions, while red hexagons represent the median values as a function of the quantity on the x-axis. In each panel we report the values of the Spearman rank correlation coefficient (and its error). The 16th–84th percentiles are shown as a red shaded area. The quantities considered on the x-axis are a) equivalent width of H α in emission, b) sSFR surface density, defined as the ratio between the SFR surface density obtained from dust attenuation corrected H α (assuming a fully sampled IMF) and the stellar mass surface density measured from MUSE data via spectral fitting (Σ_{\star}), c) H α luminosity per unit area corrected for dust attenuation with the Balmer decrement ($I_{\text{H}\alpha, \text{corr}}$), d) $E(B - V)$ of the gas obtained from the Balmer decrement, e) ratio of the luminosity per unit area in F2100W to that in F200M ($I_{21}/I_{2.0}$), f) luminosity per unit area in F2100W, g) MUSE stellar mass surface density from fits to the stellar population to optical spectra, h) molecular gas surface density, derived from ALMA CO(2-1), i) gas-phase metallicity, j) ionisation parameter, k) [S II] $\lambda\lambda 6717, 31/\text{H}\alpha$ ratio, and l) [O I] $\lambda 6300/\text{H}\alpha$ ratio.

$I_{\text{H}\alpha}$ and I_{21} in H II regions (Fig. 3). The two quantities show an excellent correlation. A linear fit to log quantities is performed by using the Bayesian framework described in Kelly (2007) which takes into account the errors on both variables. This leads to a sub-linear slope (0.91) and residual scatter around the best-fit relation of 0.26 dex.

If one corrects the H α emission for dust attenuation via the Balmer decrement, we obtain a relation with lower scatter (0.21 dex), but still a sub-linear slope of 0.85 (Fig. 3, middle panel). In this space, however, the best-fit relation (blue line) deviates from the observed data for regions of high surface brightness. This result may be compared with Leroy et al. (2023b), who analyse most of the area in each galaxy, therefore including diffuse emission, and obtain a slope of 0.77 (inverse of their reported slope

of 1.29 fitting the $I_{\text{H}\alpha}$ as a function of I_{21}). For H II regions, at $\log(I_{\text{H}\alpha}/\text{erg s}^{-1} \text{ kpc}^{-2}) > 39.0$ the relation approaches a linear slope (black line). Since bright H II regions also show higher values of dust attenuation, we interpret this as indicating that, when obscured SFR is dominant, both $I_{\text{H}\alpha, \text{corr}}$ and I_{21} are good proxies for the total ionising photon production rate.

Finally, we show the relation between $I_{\text{H}\alpha, \text{corr}}$ and the hybrid 21 μm and H α tracer (Eq. 4) using the constant a_{21}^{C07} value. In this case the quantities on the two axes show correlated errors and we take the non-diagonal elements of the covariance matrix into account to perform the fit, as described in Kelly (2007). The effect of covariance between the x- and y-axes is small in our case, with an average correlation coefficient of 0.02. Performing a fit to the log quantities, we obtain a power law slope of 0.85 and scatter

of the residuals of 0.10 dex. The hybrid tracer therefore provides an excellent match to the Balmer decrement-corrected $H\alpha$, but the resulting relation is still not linear. In particular, comparing the best-fit line (dashed blue) with the one-to-one line (black) the calibration leads to an overestimate of the dust correction at low $H\alpha$ surface brightness and a slight underestimate for the high end.

A local background subtraction leads to relations that are closer to linear, but suffer from larger scatter (e.g. a slope of 1.03 for the relation between $I_{H\alpha, \text{corr}}$ and the hybrid 21 μm and $H\alpha$, and a scatter of 0.37 dex). The deviation from linearity at low $H\alpha$ surface brightness is less evident, but still present. Because of the difficulty to provide a robust measure of the background, especially for faint regions, we do not further pursue this calculation.

3.1.3. Secondary dependencies of the calibration coefficient for 21 μm emission

In this section we test whether an additional physical parameter drives the deviation from linearity observed using a constant a_{21} coefficient. We assume that the Balmer decrement traces dust attenuation across our sample (i.e. that we do not see any fully embedded emission) and calculate the a_{21} coefficient using equation 5. For ease of benchmarking we consider the ratio between the inferred a_{21} and the C07-equivalent value of a_{21}^{C07} .

Fig. 4 shows $a_{21}/a_{21}^{\text{C07}}$ as a function of several H II region properties derived either in this work or in Groves et al. (2023). In several of the panels in Fig. 4 the quantities on the x- and y-axis are not statistically independent. We have checked, however, that analytical propagation of the error correlations implies a degree of correlation much smaller (on average 2 dex smaller) than that observed in the data: i.e. the observed trends cannot be explained by covariance among the errors alone.

We quantify the correlations between each set of quantities via the Spearman rank correlation coefficient. In order to estimate the error on this statistic we perform a Monte Carlo simulation by adding Gaussian noise to the data. We take into account the correlations between the errors on the x- and y-axis by sampling from a 2D Gaussian with the appropriate covariance matrix for each data point. The median and standard deviations of 1000 Monte Carlo runs are taken as our best estimates of the Spearman rank correlation coefficient and its error, and are shown in the top-left for each panel in Fig. 4. Given the relatively high signal-to-noise ratio in H II regions and the large dynamic range spanned in most quantities with respect to their errors, the errors on the correlation coefficients are found to be small (~ 0.01 in all panels).

The inferred a_{21} coefficient demonstrates significant positive correlations with $\text{EW}(H\alpha)$ ($\rho = 0.65$, panel a), sSFR estimated from the attenuation-corrected $H\alpha$ ($\rho = 0.64$, panel b), attenuation-corrected $H\alpha$ surface brightness ($I_{H\alpha, \text{corr}}$, $\rho = 0.60$, panel c), $E(B-V)$ computed from the Balmer decrement ($\rho = 0.55$, panel d), and the ratio of 21 μm to 2.0 μm surface brightness, where the surface brightness at 2.0 μm is taken from the NIRCам imaging data in the F200W filter ($\rho = 0.37$, panel e). $\text{EW}(H\alpha)$, sSFR, and $I_{21}/I_{2.0}$ trace the luminosity of the H II region with respect to that of the old stars. $E(B-V)$ is known to correlate with both attenuation-corrected $H\alpha$ (e.g. Emsellem et al. 2022), and $\text{EW}(H\alpha)$ (Groves et al. 2023). Overall, these trends suggest that a_{21} is slightly higher than the Calzetti et al. (2007) value for the brightest (and dustiest H II regions), while it should

Band	$\log(I_{\text{band}}/I_{21})$		
	Median	16 th perc.	84 th perc.
F335M _{PAH}	-0.38	-0.62	-0.19
F770W	0.65	0.53	0.73
F1000W	0.09	-0.04	0.17
F1130W	0.59	0.44	0.68

Table 3. Median (and 16th and 84th percentiles) of the ratio between the F335M_{PAH}, F770W, F1000W, F1130W to the F2100W luminosity (in units of $\text{erg s}^{-1} \text{kpc}^{-2}$) for the H II regions in our sample. The dependence of the I_{band}/I_{21} on $\text{EW}(H\alpha)$ is shown in Fig. 7.

be significantly lower, by up to 1.0 dex for faint, less dusty regions. All these correlations flatten for the brightest H II regions.

Substantially weaker correlations (with $|\rho| < 0.3$) are found as a function of I_{21} (panel f), stellar mass surface density (panel g), molecular gas surface density (panel h), gas-phase metallicity (panel i), or ionisation parameter (the ratio between the ionising photon flux and the hydrogen density in H II regions, panel j).

Finally, the relation between a_{21} and $[\text{S II}]\lambda\lambda 6717, 31/H\alpha$ (panel k) or $[\text{O I}]\lambda 6300/H\alpha$ (panel l) is flat at low values of these line ratios, but shows a strong negative correlation ($\rho = -0.48$ and $\rho = -0.50$, respectively) for higher ones. These line ratios have been studied in our sample by Belfiore et al. (2022) and are found to increase with decreasing $H\alpha$ surface brightness, corresponding to the transition between H II regions and diffuse ionised gas (Haffner et al. 2009; Zhang et al. 2017). Even though we are focusing on H II regions here, we are likely seeing the increased contribution of the diffuse ionised gas background to the flux within the masks corresponding to faint H II regions going hand in hand with an increase in the relative significance of the 21 μm background.

We have tested the effect of defining a local background subtraction, which leads to an increase in the scatter and a decrease in the strength of all correlation coefficients, but does not change the shape and sign of the strongest ones.

3.2. Using PAH-tracing bands to measure obscured star formation

In this section we test the ability of PAH-dominated bands to trace the obscured component of star formation. We consider the continuum-subtracted F335M NIRCам band (F335M_{PAH}), and the MIRI bands centred at 7.7 μm (F770W), 10 μm (F1000W), and 11.3 μm (F1130W). Emission in the 7.7 μm and 11.3 μm bands is dominated by features generally associated with PAHs (Smith et al. 2007; Draine & Li 2007), while the star-light contamination in the F335M band is removed as described in Sec. 2.1 and Sandstrom et al. (2023b). The nature of the continuum emission underlying the PAH features and dominating the 10 μm band emission remains unclear (Smith et al. 2007; Li 2020). Leroy et al. (2023b) find that the 10 μm continuum closely follows the PAH-dominated bands, rather than the 21 μm emission. In this work we therefore refer collectively to F335M_{PAH}, F770W, F1000W, and F1130W as ‘PAH-tracing’ bands.

3.2.1. PAH-tracing band ratios in H II regions

We adopt an empirical strategy to set fiducial values of the hybridisation coefficients for each band, a_{band} . We calculate these coefficients, which we refer to as ‘C07-equivalent’, by scaling the value of the Calzetti et al. (2007) 21 μm coefficient using the

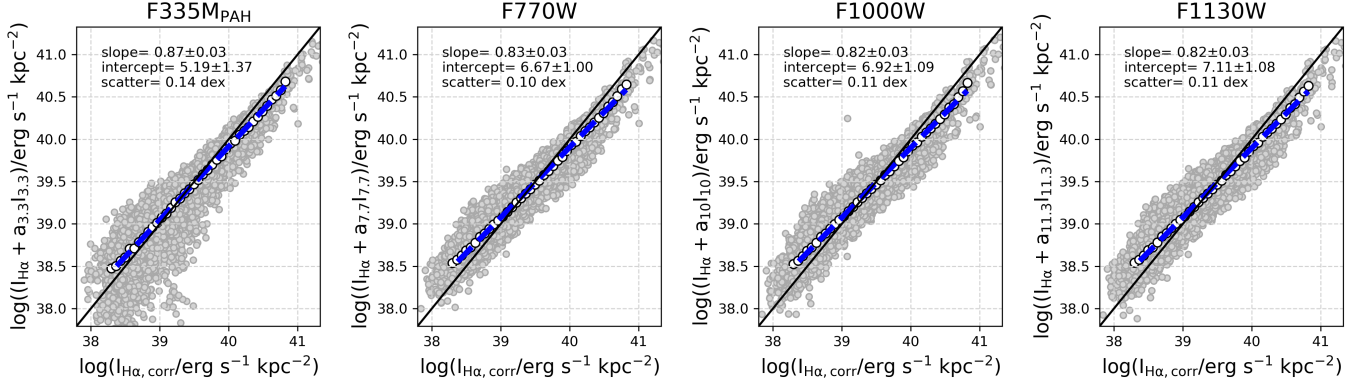


Fig. 5. Comparison of $H\alpha$ hybridised with F335M_{PAH}, F770W, F1000W and F1130W and the attenuation-corrected $H\alpha$ obtained using the Balmer decrement. The dashed blue line is the best linear fit while the white circles represent a binned average. The slope and intercept of the best-fit power law together with the scatter with respect to the best model are reported on the top left corner. The solid black line represents the one-to-one relation.

average band ratio between PAH-tracing bands and F2100W. In detail, we define

$$\log(a_{\text{band}}^{\text{C07}}) \equiv \log(a_{21}^{\text{C07}}) - \langle \log(I_{\text{band}}/I_{21}) \rangle, \quad (6)$$

where $\langle \log(I_{\text{band}}/I_{21}) \rangle$ is the median band ratio between the bands of interest (3.3, 7.7, 10, and 11.3 μm) and 21 μm in our $H\text{II}$ region sample. We report the median, 16th, and 84th percentiles of the distribution of I_{band}/I_{21} in Table 3. The scatter in the I_{band}/I_{21} lies in the range of 0.2 dex (F770W) to 0.4 dex (F335M_{PAH}). Part of this larger scatter for F335M_{PAH} may be attributed to residuals in the continuum subtraction.

3.2.2. $H\text{II}$ region scaling relations for PAH-tracing bands

Fig. 5 shows the relations between $H\alpha$ corrected using the Balmer decrement and the $H\alpha$ hybridised with each of the PAH-dominated bands using the $a_{\text{band}}^{\text{C07}}$ factor defined in Eq. 6. For all bands considered we obtain a best-fit power law with sub-linear slopes (ranging from 0.82 to 0.87, but all consistent with each other within the errors) and ~ 0.10 dex scatter (except for F335M_{PAH} for which we obtain a marginally larger scatter of 0.14 dex).

These results are remarkably consistent with those obtained with F2100W in Sec. 3.1.2. In fact, Fig. 5 demonstrates that the hybrid recipe overestimates the dust correction at low surface brightness levels ($\log(I_{H\alpha, \text{corr}}/\text{erg s}^{-1} \text{ kpc}^{-2}) < 39$), while underestimating it at high surface brightness levels, as already observed for F2100W.

3.2.3. Secondary relations of a_{band} for PAH-tracing bands

In Fig. 6 we show the median trends of the a_{band} coefficients for different bands as a function of $\text{EW}(H\alpha)$. The values of a_{band} are scaled logarithmically and normalised, so that the zero on the y-axis corresponds to the C07-equivalent value. The trend for F2100W (purple) was already presented in Fig. 4, but here we compare it directly with the behaviour of the other bands. For $\log \text{EW}(H\alpha)/\text{\AA} < 1.5$ (or $\log(\text{sSFR}/\text{yr}^{-1}) < -10$) all bands follow a closely matching trend of increasing a_{band} with $\text{EW}(H\alpha)$, reaching the C07-equivalent value at $\log \text{EW}(H\alpha)/\text{\AA} \sim 1.5$.

At high $\text{EW}(H\alpha)$, on the other hand, the behaviour of different bands diverges. The dependence of a_{21} on $\text{EW}(H\alpha)$ flattens for $\log \text{EW}(H\alpha)/\text{\AA} > 2$, plateauing to a constant value of a_{21} that

is 0.16 dex higher than the C07-equivalent one. The F335M_{PAH} band also shows a flattening in the slope of the relation but with no plateau, while F770W, F1000W, and F1130W follow increasing trends.

The difference between the PAH-tracing bands reflects the relative brightness of different features in the MIR spectrum. For example, Chasten et al. (2023b) find that the ratio of $(I_{7.7} + I_{11.3})/I_{21}$, which traces PAH abundance (Draine et al. 2021), is relatively constant in the diffuse ISM, but decreases in bright $H\text{II}$ regions. Egorov et al. (2023) find that this ratio in $H\text{II}$ regions anti-correlates with the ionisation parameter, which is tracing the density of the extreme UV photons in the region. Moreover, Chasten et al. (2023a) find that the F335M_{PAH} band is enhanced and the F1130W band is suppressed in regions of high $H\alpha$ surface brightness. These trends indicate that the abundance of PAHs is lowered in $H\text{II}$ regions, due to their destruction by extreme UV photons, but also imply changes in the average properties of the PAH population, namely a decrease in average size and an increased abundance of charged grains and/or hotter grains.

We show the change in the I_{band}/I_{21} ratios as a function of $\text{EW}(H\alpha)$ in Fig. 7. The ratio for each band is normalised by subtracting the median value for the sample, allowing for easier comparison of the trend across bands. Fig. 7 shows the expected decrease in the ratios of $I_{7.7}/I_{21}$, I_{10}/I_{21} , and $I_{11.3}/I_{21}$ as a function of $\text{EW}(H\alpha)$. $I_{7.7}/I_{21}$ shows a slightly shallower slope than I_{10}/I_{21} and $I_{11.3}/I_{21}$. The $I_{3.3}/I_{21}$ ratio, on the other hand, shows a much flatter (and even increasing) trend, with only a small decrease in the median ratio for $\log(\text{EW}(H\alpha)/\text{\AA}) > 1.8$.

4. Discussion

This work presents an unprecedented set of resolved IR data for star-forming regions at ~ 100 pc scales. Our results show the promise, and caveats, involved in the use of hybrid SFR indicators on the scales of $H\text{II}$ regions. In particular, we use IR observations with JWST at 3.3, 7.7, 10, 11.3, and 21 μm to correct $H\alpha$ emission from $H\text{II}$ regions for dust attenuation using a hybrid recipe. Using a scaled version of the C07 coefficient (Eq. 6) leads to hybrid SFR estimations which agree with the SFR derived via the Balmer decrement to within ~ 0.1 dex, but show systematic deviations for both low and high SFR. These devia-

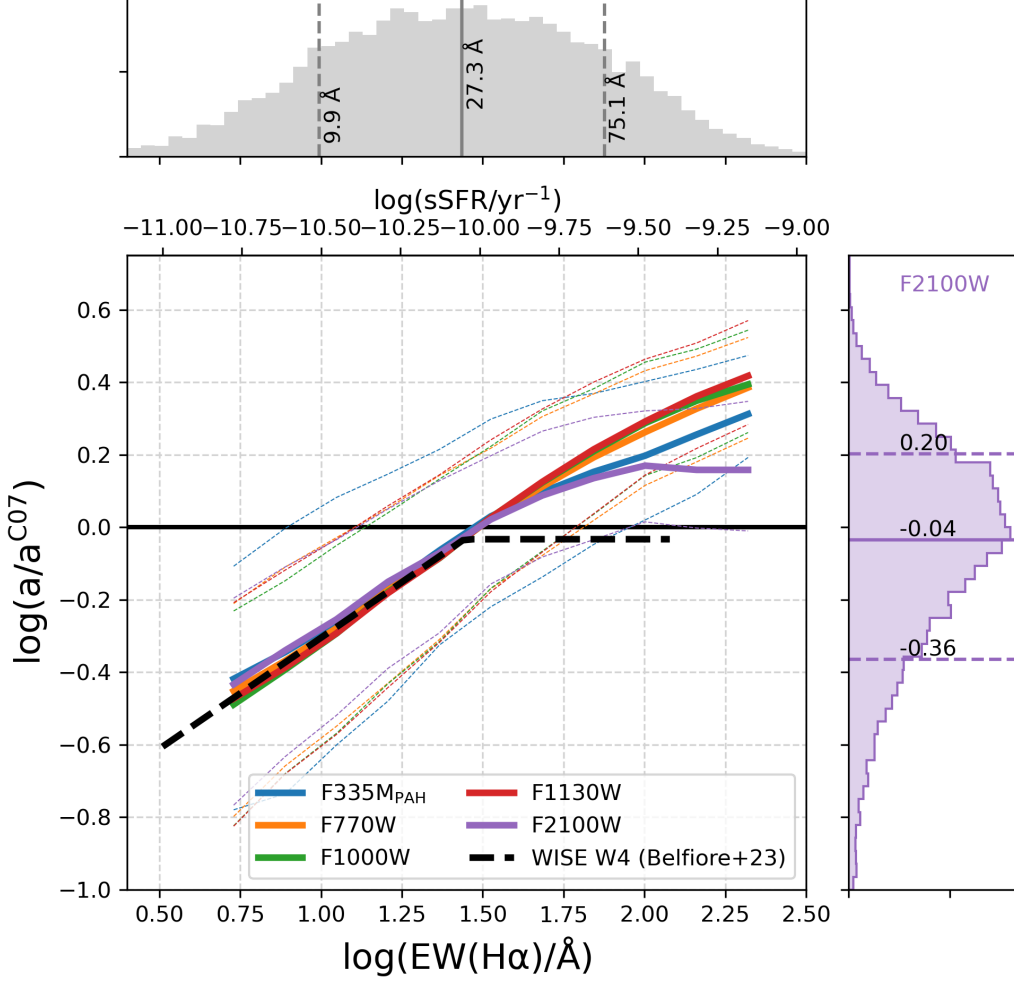


Fig. 6. $\log a_{\text{band}}$ normalised to the C07-equivalent values as a function of $\text{EW}(\text{H}\alpha)$ and sSFR (alternative x-axis on top) for H II regions in our sample, where band = [F335M_{PAH} (blue), F770W (orange), F1000W (green), F1130W (red), F2100W (purple)]. The coloured solid lines represent the median relations, while the coloured dashed lines show the 16th and 84th percentiles of the distribution. The black dashed line is the best-fit to the low-resolution (kpc-scale) $\text{H}\alpha$ + WISE W4 data from Belfiore et al. (2023). The grey histogram (top) shows the distribution of $\text{EW}(\text{H}\alpha)$ in the H II regions used in this work (with 16th, 50th, 84th percentiles marked and labelled). The purple histogram (right) shows the distribution of $\log a_{21}/a_{21}^{\text{C07}}$ for the region in our sample, with the 16th, 50th, 84th percentiles marked and labelled.

		F335M _{PAH}	F770W	F1000W	F1130W	F2100W
constant coeff. C07	$a_{\text{band}}^{\text{C07}}$	0.078	0.0077	0.027	0.0087	0.034
median measured	a_{band}	$0.079^{+0.08}_{-0.05}$	$0.0072^{+0.007}_{-0.004}$	$0.026^{+0.028}_{-0.015}$	$0.0082^{+0.009}_{-0.005}$	$0.031^{+0.023}_{-0.017}$
median measured (backg. subtracted)	$a_{\text{band}}^{\text{bkg sub}}$	$0.13^{+0.20}_{-0.08}$	$0.017^{+0.03}_{-0.01}$	$0.06^{+0.1}_{-0.04}$	$0.020^{+0.04}_{-0.014}$	$0.051^{+0.07}_{-0.03}$

Table 4. Hybridisation coefficients for various JWST bands. The top row shows the value of the Calzetti et al. (2007) coefficient, originally derived from Spitzer 24 μm , re-scaled using the median band ratios (see text). The second and third rows show the median a_{band} obtained in our sample of H II regions before and after applying a local background subtraction.

tions correlate most notably with quantities tracing sSFR (e.g., $\text{EW}(\text{H}\alpha)$).

4.1. Recommendation for using constant a_{band}

We report in Table 4 the median values of the a_{band} coefficients for our full sample of 16 474 H II regions, together with the C07-equivalent values. Our median a_{band} are in excellent agreement with the C07-equivalent values, but the scatter around these values (quantified as the 16th and 84th percentiles) are large.

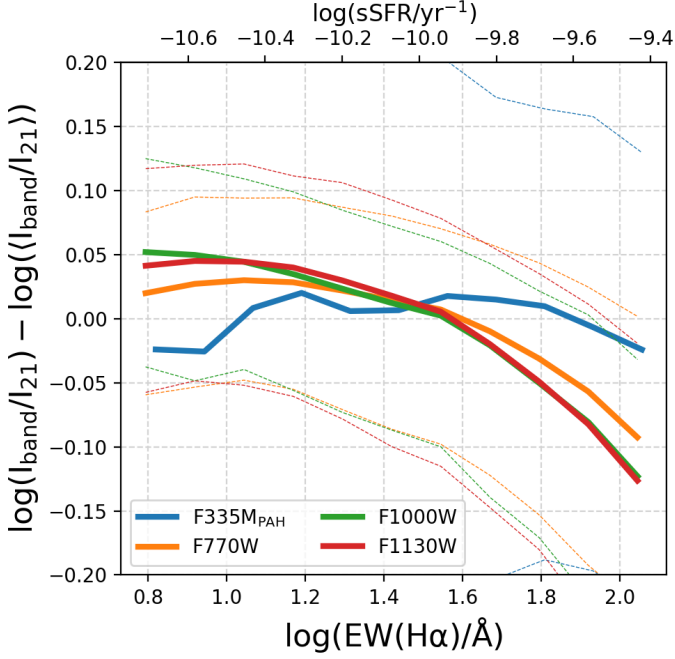


Fig. 7. The ratio of I_{band}/I_{21} normalised to the sample mean ($\langle I_{\text{band}}/I_{21} \rangle$) as a function of $\text{EW}(\text{H}\alpha)$, for band = [F335M_{PAH} (blue), F770W (orange), F1000W (green), F1130W (red)]. The solid lines represent the median, while the dashed lines correspond to the 16th and 84th percentiles. The alternative x-axis on top shows the sSFR associated with each $\text{EW}(\text{H}\alpha)$ value. The median trends show that $I_{3.3}/I_{21}$ does not show the same decrease with $\text{EW}(\text{H}\alpha)$ as the ratios of the other PAH bands.

In Table 4 we also present the median values of the a_{band} coefficients after performing a local background subtraction. These values are 0.22 to 0.38 dex larger than our nominal ones. The background subtraction more strongly affects the F770W, F1000W, and F1130W bands (a increases by ~ 0.4 dex), while it has a smaller effect on F2100W and F335M_{PAH} (a increases by ~ 0.2 dex).

The agreement between our values and the C07-equivalent ones is not immediately expected. Calzetti et al. (2007) estimate the background in large sub-galactic regions, but not using local annuli, therefore likely resulting in an intermediate estimate of the value of the background level. However, the median a_{band} will also depend on the distribution of $\text{EW}(\text{H}\alpha)$ in the sample of regions considered and on the median spatial resolution.

In fact, Fig. 6 demonstrates that the plateau observed using kpc-resolution IR data (WISE 22 μm in Belfiore et al. 2023) is a resolution effect, due to the blending of different H II regions with each other and with the diffuse medium. The trend observed by Belfiore et al. (2023) using kpc, 15''-resolution WISE W4 22 μm data and the full PHANGS-MUSE galaxy sample, is shown as the black dashed line in Fig. 6. JWST F2100W observations, providing a factor of ~ 15 higher spatial resolution than WISE W4, reveal that the relation between a_{21} and $\text{EW}(\text{H}\alpha)$ plateaus at higher $\text{EW}(\text{H}\alpha)$ (and a_{21}) than seen in the low-resolution data. Since our observations resolve the inter-cloud distance (~ 100 pc, Kim et al. 2022), and the contamination from the diffuse background is minimal for the bright regions, we expect the trend uncovered by JWST to persist at even higher spatial resolution. This hypothesis can be tested with upcoming JWST observations of more nearby (or Local Group) galaxies.

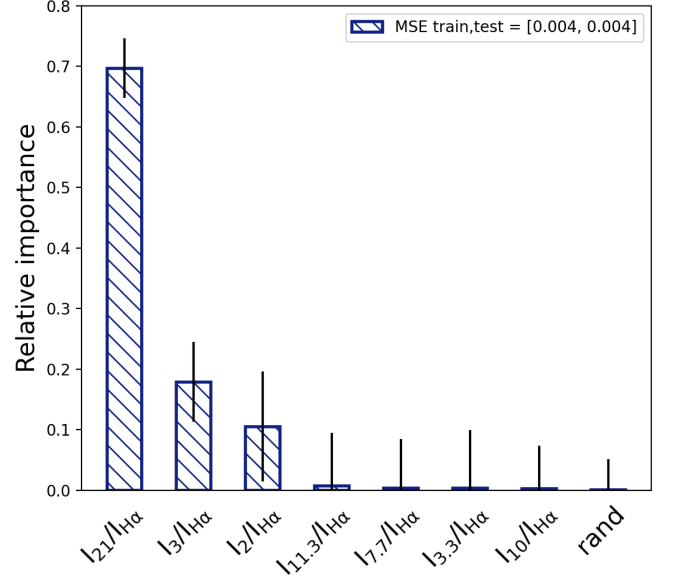


Fig. 8. Relative importance of different band ratios in predicting the $E(B-V)$ of H II regions using a random forest model. The error-bars are obtained by bootstrap random sampling. The mean squared errors (MSE) are shown for both the testing and the training set. $I_{21}/I_{\text{H}\alpha}$ and $I_{2.0}/I_{\text{H}\alpha}$ account for most of the variance in the data.

Finally, we note that our background subtraction strategy does not remove the trend of increasing a_{band} with $\text{EW}(\text{H}\alpha)$. Future work may consider more advanced approaches to model the background and test whether such contamination can explain the behaviour observed in Fig. 6 at low $\text{EW}(\text{H}\alpha)$.

4.2. Modelling the impact of old stellar population on a_{band}

The trend of increasing a_{band} with $\text{EW}(\text{H}\alpha)$ likely reflects the increasing contribution from dust heated by old stellar populations in fainter regions (Cortese et al. 2008; Leroy et al. 2012; Boquien et al. 2016; Nersesian et al. 2019), and, for the PAH-tracing bands, the roughly constant band ratios in diffuse regions (Chastenet et al. 2019).

Modelling the behaviour of a_{band} as a function of $\text{EW}(\text{H}\alpha)$, or one of the other parameters studied in Sec. 3.1.3, would provide a more accurate estimate of the dust-attenuated star formation, and a prescription more readily applicable to lower-resolution data. Several authors have presented calibrations including such additional terms, for example colours, sSFR, or M_{\star} (Boquien et al. 2016; Zhang & Ho 2023; Belfiore et al. 2023; Kouroumpatzakis et al. 2023).

We aim to provide such a second-order correction applicable to nearby galaxies data. The functional form that this correction should take is not evident a priori. For the sake of simplicity, here we add an additional linear term to the conventional hybrid star formation recipe presented in Eq. 4, leading to

$$I_{\text{H}\alpha, \text{corr}} = I_{\text{H}\alpha} + \alpha I_{\text{IR}} + \beta I_Q, \quad (7)$$

where I_{IR} is one of the JWST IR dust-tracing bands, and I_Q is a second physical quantity appropriately chosen to best reproduce the extinction correction from the Balmer decrement. As before, we express all surface brightness measurements in units of $\text{erg s}^{-1} \text{kpc}^{-2}$.

We first consider the task of deriving an estimate for the obscured SFR using two JWST bands: a dust-tracing band

(F2100W or any of the PAH-tracing bands), and a second band tracing stellar continuum emission (F200W, F300M or F360M) to account for the dust heating from old stars. To determine the best combination of bands for such a calibration we run a random forest regression, using the algorithm implementation in `SCIKIT-LEARN` (Pedregosa et al. 2011). In particular, we use the random forest model to determine the relative importance of input features (Bluck et al. 2022; Baker et al. 2022). This approach is conceptually similar to more traditional principal component analysis, but allows the generation of more complex, non-linear models.

The random forest algorithm is a form of supervised machine learning that builds a non-parametric model using multiple decision trees, trained to decrease the Gini impurity at each split. We use $E(B-V)$ as the target variable since the goal is to understand how best to perform the dust correction, and $I_{\text{band}}/I_{\text{H}\alpha}$, where ‘band’ is one of the JWST bands available to us (F200W, F300M, F360M, F335M_{PAH}, F770W, F1000W, F1130W, F2100W), as input features. We also consider an array of random numbers as an additional input feature to test the performance of the algorithm. The dataset is subdivided into a training (80% of the full sample) and testing (remaining 20%) subset of H II regions. Only H II regions covered by both NIRCам and MIRI and with signal-to-noise ratio greater than 3 in all JWST bands are used for this computation. After training, the mean square error (MSE) of the test set is compared with that of the training sample in order to check the quality of the resulting model and avoid overfitting.

We find that the combination of $I_{21}/I_{\text{H}\alpha}$ and $I_{3,0}/I_{\text{H}\alpha}$ accounts for nearly all the variance in $E(B-V)$ (Fig. 8). Once these two variables are taken into account, the remaining ones have residual importance consistent with random within the errors. The MSE of the training and test set are comparable (reported on the top right of Fig. 8), demonstrating that the algorithm produced a successful model. This analysis confirms two of the key insights from this work: 1) F2100W is the best band to use for hybridisation among the bands tracing dust emission available in our PHANGS–JWST filter set, and 2) there exists an evident secondary dependence on the mass-tracing NIRCам bands, of which the best is F300M.

Having established I_{21} and $I_{3,0}$ as the two best variables, we fit the extinction-corrected $\text{H}\alpha$ surface brightness with a two-parameter regression model, using the Bayesian formalism discussed in Hogg et al. (2010). We fit for the α and β parameters in Eq. 7 and for intrinsic scatter in the relation, using the Bayesian Monte Carlo sampler `EMCEE`, and obtain best-fit as relation

$$I_{\text{H}\alpha,\text{corr}} = I_{\text{H}\alpha} + 0.026 I_{21} - 0.0011 I_3, \quad (8)$$

We also fit using the F200W and F360M NIRCам bands, obtaining respectively $\alpha = 0.026$, $\beta = 4.2 \times 10^{-4}$, and $\alpha = 0.025$, $\beta = -0.001$.

Our approach here is similar to the one of Kouroumpatzakis et al. (2023), who use spectral energy distribution models generated with the code `CIGALE` to study how best to determine SFR from JWST bands. In their work, however, Kouroumpatzakis et al. (2023) do not consider $I_{\text{H}\alpha}$, but model the SFR as a linear combination of I_{21} and $I_{2,0}$. Their results are therefore not directly comparable. We leave a direct comparison of our results with spectral energy distribution models to future work.

Finally, we repeat our two-parameter fit using stellar mass surface density Σ_* , which may be used in the absence of JWST NIRCам data. We obtain

$$I_{\text{H}\alpha,\text{corr}} = I_{\text{H}\alpha} + 0.028 I_{21} - 0.085 \times 10^{31} \Sigma_*, \quad (9)$$

where surface brightnesses are in units of $\text{erg}^{-1} \text{s}^{-1} \text{kpc}^{-2}$ and Σ_* is in units of $\text{M}_\odot \text{kpc}^{-2}$.

4.3. Does the IR emission trace embedded SFR or cold gas?

The MIR, and in particular the bands containing strong PAH features, show excellent correlations with the cold molecular gas content, mapped by CO emission (Regan et al. 2006; Chown et al. 2021; Whitcomb et al. 2022; Leroy et al. 2023a). Leroy et al. (2021b) and Leroy et al. (2023a), for example, found a nearly linear relation between the intensity in the WISE W3 band centred at $12 \mu\text{m}$ and CO(2-1) emission. This correlation is found to have lower scatter than that between CO and IR emission at $\sim 24 \mu\text{m}$. Whitcomb et al. (2022) similarly argued using correlation analysis that emission around $12 \mu\text{m}$ traces CO emission better than SFR, while IR emission at $24 \mu\text{m}$ traces SFR better than CO. Leroy et al. (2023b) use the early JWST data for four galaxies from our sample and compare the MIR emission with both $\text{H}\alpha$ and CO emission, finding that MIR emission correlates well with both extinction-corrected $\text{H}\alpha$ and CO. Such a result is expected, since dust emission depends on both the dust surface density and the intensity of the radiation field heating it. The convolution of these effects leads to MIR emission being a useful tracer of both $I_{\text{H}\alpha,\text{corr}}$ and CO.

Within H II regions, however, one expects a tighter relation between MIR emission and star formation than between MIR emission and cold gas content. To test this hypothesis we evaluate the relative ability of each of the JWST bands considered in this work to trace extinction-corrected $\text{H}\alpha$, molecular gas (as traced by CO(2-1)), and stellar mass surface density, focusing our analysis on H II regions specifically. The analysis is performed by building a random forest regression model for the surface brightness in each JWST band and using $I_{\text{H}\alpha,\text{corr}}$, I_{CO} , and Σ_* , in addition to a vector of random numbers, as input features. The relative importance of each of the features in reproducing the brightness in each JWST band considered is presented in Fig. 9.

As expected, both F300M and F200W trace mostly stellar mass surface density (importance $\sim 90\%$). For F360M $\text{H}\alpha$ takes up part of the importance, probably reflecting the increasing importance of hot dust and residual contamination from PAHs in this band (Sandstrom et al. 2023a). F335M_{PAH} mostly traces $\text{H}\alpha$, highlighting the success of the continuum subtraction strategy for this band. The MIR bands trace mostly $\text{H}\alpha$, but with 15-20% importance attributed also to CO for F770W, F1000W, F1130W. The contribution of stellar mass is small, and it is largest at F1000W, where it amounts to 7% of the overall importance. This band contains the largest contamination from point sources, potentially evolved stars, whose density correlates with the overall stellar mass surface density. For the canonical F2100W band the relative importance of $\text{H}\alpha$ and CO are 81% and 16% respectively. In summary, both $3.3 \mu\text{m}$ and the MIR bands trace mostly extinction-corrected $\text{H}\alpha$ within H II regions, with a smaller ($<20\%$) secondary dependence on molecular gas, as traced by CO. The small dependence on CO is consistent with the finding that many H II regions exist without associated molecular gas, in the sense of gas within the H II region boundary (Zakardjian et al. 2023). These conclusions are likely to differ within the more diffuse medium, where the relative importance of CO in determining the MIR emission is expected to increase (Leroy et al. 2023b), but we leave an exploration of these trends to future work.

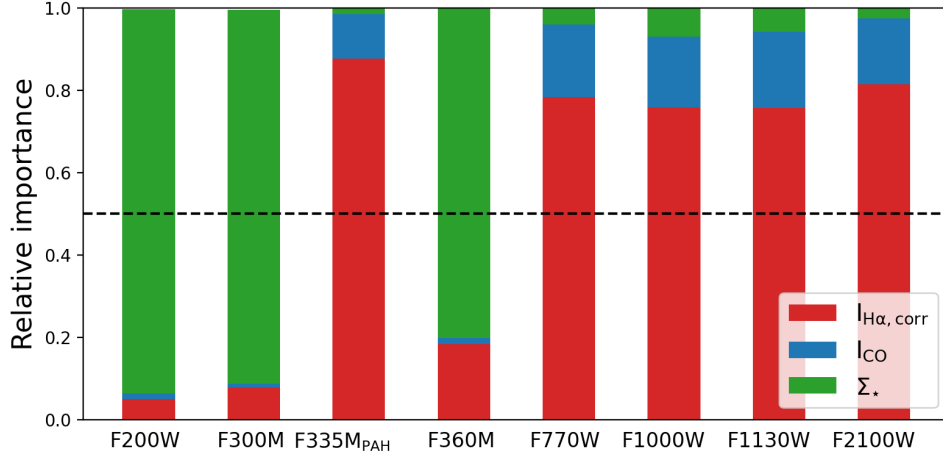


Fig. 9. Relative importance of extinction-corrected $H\alpha$ ($I_{H\alpha,corr}$), CO(2-1) surface density, and stellar mass surface density (Σ_*) in predicting the surface brightness of $H II$ regions in a set of JWST bands.

5. Conclusions

We use NIRCcam and MIRI images in combination with IFS from MUSE for 16 nearby galaxies to calibrate hybrid recipes to correct $H\alpha$ for dust extinction on the scales of individual $H II$ regions (~ 100 pc). We examine hybrid recipes that consider a linear combination of $H\alpha$ with the F2100W MIRI band, dominated by emission from small grains, and bands tracing PAH emission, namely the continuum-subtracted NIRCcam F335M band (F335M_{PAH}), and the F770W, F1000W, and F1130W MIRI bands. We summarise our main results below.

- The ratio between $21 \mu m$ and $H\alpha$ emission is systematically higher in the diffuse ISM, outside optically defined $H II$ regions. This fact reflects a change in the dominant source of dust heating – young stars in $H II$ regions and the old stellar population in the DIG – and not an increase in dust attenuation. Fully embedded regions make a negligible contribution to the diffuse $21 \mu m$ emission.
- Focusing on $H II$ regions, we calibrate the coefficient in front of the IR emission term ($I_{H\alpha,corr} = I_{H\alpha} + a_{band} I_{band}$) by benchmarking the hybrid dust correction recipe with the correction obtained using the Balmer decrement measured from the MUSE data. We adopt fiducial hybridisation coefficients for the different dust-tracing JWST bands (a_{band}^{C07}) by rescaling the coefficient derived by Calzetti et al. (2007) for *Spitzer* $24 \mu m$ emission by the average band ratio $\langle I_{24}/I_{band} \rangle$. These C07-equivalent coefficients are in good general agreement with the median of the measured a_{band} coefficient across our sample of $H II$ regions for all bands considered (F335M_{PAH}, F770W, F1000W, F1130W, F2100W).
- For both $21 \mu m$ and the PAH-tracing bands, using a hybrid recipe with a constant coefficient a_{band}^{C07} leads to extinction-corrected $H\alpha$ fluxes that correlate well (scatter ~ 0.1 dex), albeit sub-linearly (slope 0.82-0.87), with those inferred from the Balmer decrement. The sub-linear slope implies that a constant a_{band} overestimates the dust correction for faint $H II$ regions, and it underestimates it for bright regions.
- We tested for secondary dependencies of a_{band} on a number of additional physical parameters. The strongest correlations are with physical parameters that trace the ratio between young and old stellar components, e.g. $EW(H\alpha)$, sSFR, or indirectly correlate with them (e.g. $H\alpha$ surface brightness, or dust attenuation measured from the Balmer decrement).

Strong correlations are also found with line ratios that trace the change in the ionisation condition between $H II$ regions and DIG ($[O I]/H\alpha$, $[S II]/H\alpha$). These trends indicate that dust heating from the old stellar component contributes substantially to the IR emission for the fainter $H II$ regions in our sample.

- a_{band} correlates with $EW(H\alpha)$ for all bands considered. For $EW(H\alpha) < 30 \text{ \AA}$, the trends are similar for all bands and agree with the recent kpc-resolution study of Belfiore et al. (2023). At higher $EW(H\alpha)$, a_{21} plateaus to a constant value, while the coefficients for the F770W, F1000W, and F1130W keep increasing. The behaviour of the MIR PAH-tracing bands reflects the relative decrease in PAH emission in bright $H II$ regions, in agreement with the literature predicting the destruction of PAH molecules in such harsh environments. The F335M_{PAH} shows an intermediate behaviour between F2100W and the other MIR bands, which can be explained by the relative increase in $3.3 \mu m$ emission with respect to the other PAH-tracing bands in $H II$ regions, possibly tracing a decrease in the average size of PAH grains.
- A random forest analysis confirms that F2100W is the preferred band to consider in combination with $H\alpha$ to infer dust attenuation, confirming results from previous literature using WISE $22 \mu m$ or *Spitzer* $24 \mu m$ bands.
- The main secondary dependence of a_{band} can be modelled by explicitly adding an additional linear term proportional to stellar mass surface density or $3 \mu m$ emission to the hybrid recipe. We provide coefficients for these corrections in Eq. 8 and 9.
- Finally, we analyse the relative importance of molecular gas (traced by CO(2-1)), stellar mass surface density, and extinction-corrected $H\alpha$ in determining the surface brightness for $H II$ regions within our JWST bands. The MIR bands trace mostly $H\alpha$ but with a smaller (15-20%) importance attributed to CO.

Acknowledgements. This work is carried out as part of the PHANGS collaboration. Based on observations made with the NASA/ESA/CSA *JWST*. The data were obtained from the Mikulski Archive for Space Telescopes at the Space Telescope Science Institute, which is operated by the Association of Universities for Research in Astronomy, Inc., under NASA contract NAS 5-03127. The observations are associated with *JWST* program 2107 (PI: J. Lee) Based on observations collected at the European Southern Observatory under ESO programmes 094.C-0623 (PI: Kreckel), 095.C-0473, 098.C-0484 (PI: Blanc), 1100.B-0651 (PHANGS-MUSE; PI: Schinnerer), as well as 094.B-0321 (MAGNUM; PI: Marconi), 099.B-0242, 0100.B-0116, 098.B-0551 (MAD; PI: Car-

ollo) and 097.B-0640 (TIMER; PI: Gadotti). FB acknowledges support from the INAF Fundamental Astrophysics program 2022. MB acknowledges support from FONDECYT regular grant 1211000 and by the ANID BASAL project FB210003. HAP acknowledges support by the National Science and Technology Council of Taiwan under grant 110-2112-M-032-020-MY3. JMDK gratefully acknowledges funding from the ERC under the European Union's Horizon 2020 research and innovation programme via the ERC Starting Grant MUSTANG (grant number 714907). COOL Research DAO is a Decentralized Autonomous Organization supporting research in astrophysics aimed at uncovering our cosmic origins. MC gratefully acknowledges funding from the DFG through an Emmy Noether Research Group (grant number CH2137/1-1). RSK and SCOG acknowledge financial support from the ERC via the ERC Synergy Grant "ECOGAL" (project ID 855130), from the German Excellence Strategy via the Heidelberg Cluster of Excellence (EXC 2181 - 390900948) "STRUCTURES", and from the German Ministry for Economic Affairs and Climate Action in project "MAINN" (funding ID 500O2206). RSK also thanks for computing resources provided bwHPC and DFG through grant INST 35/1134-1 FUGG and for data storage at SDS@hd through grant INST 35/1314-1 FUGG. JC acknowledges support from ERC starting grant #851622 DustOrigin. MQ acknowledges support from the Spanish grant PID2019-106027GA-C44, funded by MCIN/AEI/10.13039/501100011033. KK, OVE and EJW gratefully acknowledge funding from the Deutsche Forschungsgemeinschaft (DFG, German Research Foundation) in the form of an Emmy Noether Research Group (grant number KR4598/2-1, PI Kreckel). JN acknowledges funding from the European Research Council (ERC) under the European Union's Horizon 2020 research and innovation programme (grant agreement No. 694343). ER and HH acknowledge the support of the Natural Sciences and Engineering Research Council of Canada (NSERC), funding reference number RGPIN-2022-03499, and the support of the Canadian Space Agency (22ASTALBER). AKL gratefully acknowledges support by grants 1653300 and 2205628 from the National Science Foundation, by award JWST-GO-02107.009-A, and by a Humboldt Research Award from the Alexander von Humboldt Foundation. KS acknowledges funding support from grant support by JWST-GO-02107.006-A

References

- Anand, G. S., Lee, J. C., Van Dyk, S. D., et al. 2021, *MNRAS*, 501, 3621
- Aniano, G., Draine, B. T., Gordon, K. D., & Sandstrom, K. 2011, *PASP*, 123, 1218
- Baker, W. M., Maiolino, R., Bluck, A. F. L., et al. 2022, 7, 1
- Baldwin, J. A., Phillips, M. M., & Terlevich, R. 1981, *PASP*, 93, 5
- Belfiore, F., Leroy, A., Sun, J., et al. 2023, *A&A*, 670, A67
- Belfiore, F., Santoro, F., Groves, B., et al. 2022, *A&A*, 659, A26
- Bendo, G. J., Boselli, A., Dariush, A., et al. 2012, *MNRAS*, 419, 1833
- Bendo, G. J., Dale, D. A., Draine, B. T., et al. 2006, *ApJ*, 652, 283
- Bluck, A. F., Maiolino, R., Brownson, S., et al. 2022, *A&A*, 659, A160
- Bolatto, A. D., Simon, J. D., Stanimirović, S., et al. 2007, *ApJ*, 655, 212
- Bolatto, A. D., Wolfire, M., & Leroy, A. K. 2013, *ARA&A*, 51, 207
- Boquien, M., Kennicutt, R., Calzetti, D., et al. 2016, *A&A*, 591, A6
- Calzetti, D. 2020, *Nat. Astron.*, 4, 437
- Calzetti, D., Kennicutt, R. C., Engelbracht, C. W., et al. 2007, *ApJ*, 666, 870
- Catalán-Torrecilla, C., Gil de Paz, A., Castillo-Morales, A., et al. 2015, *A&A*, 584, A87
- Chastenet, J., Sandstrom, K., Chiang, I.-D., et al. 2019, *ApJ*, 876, 62
- Chastenet, J., Sutter, J., Sandstrom, K., et al. 2023a, *ApJL*, 944, L12
- Chastenet, J., Sutter, J., Sandstrom, K., et al. 2023b, *ApJL*, 944, L11
- Chown, R., Li, C., Parker, L., et al. 2021, *MNRAS*, 500, 1261
- Cortese, L., Boselli, A., Franzetti, P., et al. 2008, *MNRAS*, 386, 1157
- Crocker, A. F., Calzetti, D., Thilker, D. A., et al. 2013, *ApJ*, 762, 79
- De Looze, I., Fritz, J., Baes, M., et al. 2014, *A&A*, 571, 1
- Den Brok, J. S., Chatzigiannakis, D., Bigiel, F., et al. 2021, *MNRAS*, 504, 3221
- Diaz, A. I., Terlevich, E., Vázquez, J. M., et al. 1991, *MNRAS*, 253, 245
- Draine, B. T. & Li, A. 2007, *ApJ*, 657, 810
- Draine, B. T., Li, A., Hensley, B. S., et al. 2021, *ApJ*, 917, 3
- Egorov, O. V., Kreckel, K., Sandstrom, K. M., et al. 2023, *ApJ*, 944, L16
- Emsellem, E., Schinnerer, E., Santoro, F., et al. 2022, *A&A*, 659, A191
- Galliano, F., Galametz, M., & Jones, A. P. 2018, *ARA&A*, 56, 673
- Groves, B., Krause, O., Sandstrom, K., et al. 2012, *MNRAS*, 426, 892
- Groves, B., Kreckel, K., Santoro, F., et al. 2023, *MNRAS*, 520, 4902
- Gruppioni, C., Pozzi, F., Rodighiero, G., et al. 2013, *MNRAS*, 432, 23
- Haffner, L. M., Dettmar, R.-J. J., Beckman, J. E., et al. 2009, *Rev. Mod. Phys.*, 81, 969
- Hao, C. N., Kennicutt, R. C., Johnson, B. D., et al. 2011, *ApJ*, 741, 124
- Hassani, H., Rosolowsky, E., Leroy, A. K., et al. 2023, *ApJL*, 944, L21
- Helou, G., Roussel, H., Appleton, P., et al. 2004, *ApJS*, 154, 253
- Hirashita, H., Buat, V., & Inoue, A. K. 2003, *A&A*, 410, 83
- Hogg, D. W., Bovy, J., & Lang, D. 2010 [[arXiv:1008.4686](#)]
- Jarrett, T. H., Masci, F., Tsai, C. W., et al. 2013, *AJ*, 145, 6
- Kauffmann, G., Heckman, T. M., Tremonti, C., et al. 2003, *MNRAS*, 346, 1055
- Kelly, B. C. 2007, *ApJ*, 665, 1489
- Kennicutt, R. C. 1998, *ARA&A*, 36, 189
- Kennicutt, R. C., Calzetti, D., Walter, F., et al. 2007, *ApJ*, 671, 333
- Kennicutt, R. C. & Evans, N. J. 2012, *ARA&A*, 50, 531
- Kennicutt, R. C., Hao, C. N., Calzetti, D., et al. 2009, *ApJ*, 703, 1672
- Kewley, L. J., Dopita, M. A., Sutherland, R. S., Heisler, C. A., & Trevena, J. 2001, *ApJ*, 556, 121
- Kim, J., Chevance, M., Kruijssen, J. M. D., et al. 2022, *MNRAS*, 516, 3006
- Kouroumpatzakis, K., Zezas, A., Kyritsis, E., Salim, S., & Svoboda, J. 2023, [arXiv:1](#)
- Lai, T. S.-Y., Smith, J. D. T., Baba, S., Spoon, H. W. W., & Imanishi, M. 2020, *ApJ*, 905, 55
- Lang, P., Meidt, S. E., Rosolowsky, E., et al. 2020, *ApJ*, 897, 122
- Lebouteiller, V., Bernard-Salas, J., Whelan, D. G., et al. 2011, *ApJ*, 728
- Lee, J. C., Sandstrom, K. M., Leroy, A. K., et al. 2023, *ApJL*, 944, L17
- Leroy, A. K., Bigiel, F., de Blok, W. J. G., et al. 2012, *AJ*, 144, 3
- Leroy, A. K., Bolatto, A. D., Sandstrom, K., et al. 2023a, *ApJ*, 944, L10
- Leroy, A. K., Hughes, A., Liu, D., et al. 2021a, *ApJS*, 255, 19
- Leroy, A. K., Sandstrom, K., Rosolowsky, E., et al. 2023b, *ApJL*, 944, L9
- Leroy, A. K., Sandstrom, K. M., Lang, D., et al. 2019, *ApJS*, 244, 24
- Leroy, A. K., Schinnerer, E., Hughes, A., et al. 2021b, *ApJS*, 257, 43
- Leslie, S. K., Schinnerer, E., Groves, B., et al. 2018, *A&A*, 616, 1
- Li, A. 2020, *Nat. Astron.*, 4, 339
- Lu, Y., Blanc, G. A., & Benson, A. 2015, *ApJ*, 808, 129
- Lutz, D., Valiante, E., Sturm, E., et al. 2005, *ApJ*, 625, L83
- Madau, P. & Dickinson, M. 2014, *ARA&A*, 52, 415
- Maragkoudakis, A., Ivkovich, N., Peeters, E., et al. 2018, *MNRAS*, 481, 5370
- Nersesian, A., Xilouris, E. M., Bianchi, S., et al. 2019, *A&A*, 624, A80
- O'Donnell, J. E. 1994, *ApJ*, 422, 158
- Osterbrock, D. E. & Ferland, G. J. 2006, *Astrophysics of Gaseous Nebulae and Active Galactic Nuclei*.
- Pedregosa, F., Varoquaux, G., Gramfort, A., et al. 2011, *JMLR*, 12, 2825
- Peeters, E., Spoon, H. W. W., & Tielens, A. G. G. M. 2004, *ApJ*, 613, 986
- Perrin, M. D., Sivaramakrishnan, A., Lajoie, C.-P., et al. 2014, *Sp. Telesc. Instrum.* 2014 Opt. Infrared, Millim. Wave, 9143, 91433X
- Phillips, M. M., Jenkins, E. B., Dopita, M. A., Sadler, E. M., & Binette, L. 1986, *AJ*, 91, 1062
- Pilyugin, L. S. & Grebel, E. K. 2016, *MNRAS*, 457, 3678
- Regan, M. W., Thornley, M. D., Vogel, S. N., et al. 2006, *ApJ*, 652, 1112
- Riechers, D. A., Pope, A., Daddi, E., et al. 2014, *ApJ*, 786, 31
- Salim, S., Boquien, M., & Lee, J. C. 2018, *ApJ*, 859, 11
- Sandstrom, K. M., Chastenet, J., Sutter, J., et al. 2023a, *ApJ*, 944, L7
- Sandstrom, K. M., Koch, E. W., Leroy, A. K., et al. 2023b, *ApJL*, 944, L8
- Shipley, H. V., Papovich, C., Rieke, G. H., Brown, M. J. L., & Moustakas, J. 2016, *ApJ*, 818, 60
- Smith, J. D. T., Draine, B. T., Dale, D. A., et al. 2007, *ApJ*, 656, 770
- Thilker, D. A., Braun, R., & Walterbos, R. A. M. 2000, *AJ*, 120, 3070
- Viaene, S., Sarzi, M., Baes, M., Fritz, J., & Puerari, I. 2017, *MNRAS*, 472, 1286
- Wetzel, K. B., Cappellari, M., Bershad, M. A., et al. 2019, *AJ*, 158, 57
- Whitcomb, C. M., Sandstrom, K., Leroy, A., & Smith, J. D. T. 2022, [ArXiv:2212.00180v1 \[arXiv:2212.00180\]](#)
- Williams, T. G., Baes, M., Looze, I. D., et al. 2019, *MNRAS*, 487, 2753
- Wuyts, S., Förster Schreiber, N. M., Lutz, D., et al. 2011a, *ApJ*, 738, 106
- Wuyts, S., Förster Schreiber, N. M., van der Wel, A., et al. 2011b, *ApJ*, 742, 96
- Zakardjian, A., Pety, J., Herrera, C. N., et al. 2023, [arXiv:2305.03650](#)
- Zhang, K., Yan, R., Bundy, K., et al. 2017, *MNRAS*, 466, 3217
- Zhang, L. & Ho, L. C. 2023, *ApJ*, 943, 60

¹ INAF — Osservatorio Astrofisico di Arcetri, Largo E. Fermi 5, I-50125, Florence, Italy e-mail: francesco.belfiore@inaf.it

² Department of Astronomy, The Ohio State University, 140 West 18th Avenue, Columbus, OH 43210, USA

³ Sub-department of Astrophysics, Department of Physics, University of Oxford, Keble Road, Oxford OX1 3RH, UK

⁴ European Southern Observatory, Karl-Schwarzschild Straße 2, D-85748 Garching bei München, Germany

⁵ Argelander-Institut für Astronomie, Universität Bonn, Auf dem Hügel 71, D-53121 Bonn, Germany

⁶ Centro de Astronomía (CITEVA), Universidad de Antofagasta, Avenida Angamos 601, Antofagasta, Chile

⁷ Max-Planck-Institut für extraterrestrische Physik (MPE), Giessenbachstrasse 1, D-85748 Garching, Germany

⁸ Sterrenkundig Observatorium, Ghent University, Krijgslaan 281-S9, 9000 Gent, Belgium

- ⁹ European Southern Observatory (ESO), Alonso de Córdova 3107, Casilla 19, Santiago 19001, Chile
- ¹⁰ Department of Physics and Astronomy, University of Wyoming, Laramie, WY 82071, USA
- ¹¹ Astronomisches Rechen-Institut, Zentrum für Astronomie der Universität Heidelberg, Mönchhofstraße 12-14, D-69120 Heidelberg, Germany
- ¹² Univ Lyon, Univ Lyon1, ENS de Lyon, CNRS, Centre de Recherche Astrophysique de Lyon UMR5574, F-69230 Saint-Genis-Laval France
- ¹³ Universität Heidelberg, Zentrum für Astronomie, Institut für theoretische Astrophysik, Albert-Ueberle-Straße 2, D-69120, Heidelberg, Germany
- ¹⁴ International Centre for Radio Astronomy Research, University of Western Australia, 7 Fairway, Crawley, 6009, WA, Australia
- ¹⁵ Universität Heidelberg, Interdisziplinäres Zentrum für Wissenschaftliches Rechnen, Im Neuenheimer Feld 205, D-69120 Heidelberg, Germany
- ¹⁶ Max-Planck-Institute for Astronomy, Königstuhl 17, D-69117 Heidelberg, Germany
- ¹⁷ Observatorio Astronómico Nacional (IGN), C/Alfonso XII, 3, E-28014 Madrid, Spain
- ¹⁸ Department of Physics, University of Alberta, Edmonton, Alberta, T6G 2E1, Canada
- ¹⁹ Departamento de Física de la Tierra y Astrofísica, Universidad Complutense de Madrid, E-28040 Madrid, Spain
- ²⁰ Instituto de Física de Partículas y del Cosmos IPARCOS, Facultad de CC Físicas, UCM, E-28040, Madrid, Spain
- ²¹ Department of Astronomy & Astrophysics, University of California, San Diego, 9500 Gilman Drive, San Diego, CA 92093, USA
- ²² Department of Physics and Astronomy, McMaster University, 1280 Main St. West, Hamilton ON L8S 4M1 Canada
- ²³ Canadian Institute for Theoretical Astrophysics (CITA), University of Toronto, 60 St George Street, Toronto, ON M5S 3H8, Canada